To cite this version :

Lucas LAPOSTOLLE, Léo MORIN, Katell DERRIEN, Laurent BERTHE, Olivier CASTELNAU -
Modeling and simulation of laser shock waves in elasto-plastic polycrystalline microstructures -
Journal of the mechanics and physics of solids - 2023

Modeling and simulation of laser shock waves in elasto-plastic polycrystalline microstructures

L. Lapostolle [a,*], L. Morin [b], K. Derrien [a], L. Berthe [a], O. Castelnau [a]

[a] PIMM, Arts et Metiers Institute of Technology, CNRS, Cnam, HESAM University, 151 Boulevard de l'Hopital, 75013 Paris, France
[b] University of Bordeaux, CNRS, Arts et Metiers Institute of Technology, Bordeaux INP, I2M Bordeaux, F-33400 Talence, France

ABSTRACT

We study the propagation of elasto-plastic shockwaves induced by high power laser impacts in 2D polycrystalline metallic alloys in order to investigate the influence of the material microstructure on the fields of plastic strain and subsequent residual stresses. Implementing a visco-plastic constitutive relation at the grain scale accounting for two dislocation slip systems into a finite volume numerical scheme, simulations on single crystal specimens with different lattice orientations show that plastic strain is concentrated in narrow bands originating at the edges of the laser impact and parallel to the slip planes. In the case of polycrystalline microstructures composed of randomly oriented grains, it is found that the microstructure morphology is the origin of a heterogeneous distribution of the residual plastic strain and stress fields, which thus departs from the residual stress fields usually modeled when the microstructure is not accounted for. To account for the random character of polycrystal microstructures, we perform a statistical analysis of the mechanical fields over a large number of microstructures to quantify the dispersion of the results. It is found that even though the residual stresses induced by a laser impact are in compression on average at the center of the laser impact, some realizations of the microstructures can lead to localized concentrations of less compressive, or even tensile, residual stresses at the surface, thus probably reducing the fatigue resistance of the shocked material.

1. Introduction

This work finds motivation in the modeling of the Laser Shock Peening (LSP) process. In this process, a high-energy laser (~ 10 GW cm^{-2}) is used to impact a metallic specimen and introduce compressive residual stresses. The laser pulse, whose duration is typically 10 ns, interacts with the surface of the material, generating a high pressure plasma (see illustration on Fig. 1). The sudden release of this plasma creates a pressure wave inside the material with an amplitude high enough to induce inhomogeneous plastic strains and subsequent residual stresses. These residual stresses have then been related to an improved fatigue behavior (Peyre et al., 1996; Ding and Ye, 2006), which makes LSP promising in aeronautical and energy industries to improve the fatigue life of structures (Clauer, 2019). The standard configuration for LSP also includes a confinement medium (usually water) to increase the pressure transmitted into the material, and a protective coating to avoid strong thermal effects (which can lead to tensile surface residual stresses) (Fox, 1974). LSP also induces huge strain rate in the material, of the order of 10^6 s^{-1}.

For more than 20 years now, laser shot peening simulations have been carried out, in research and industrial application contexts, using macroscopic and isotropic constitutive relations for the target material (Braisted, 1999; Peyre et al., 2012; Brockman et al.,
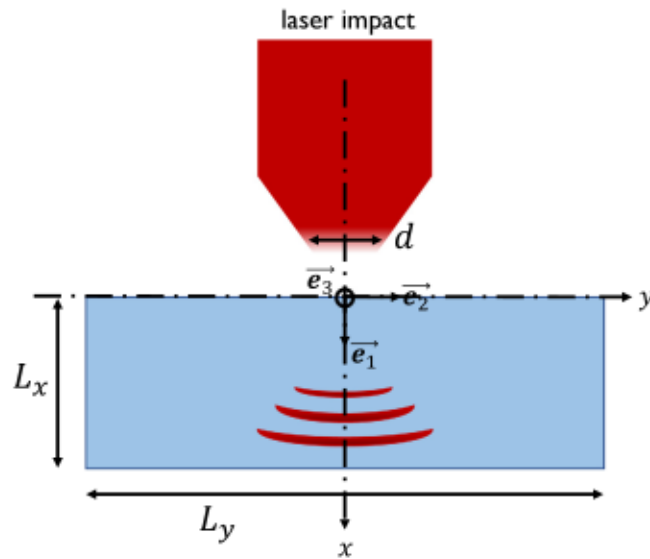
Fig. 1. Illustration of the LSP process for 2D modeling.

2012; Julan, 2015). This approach assumes that the influence of the heterogeneous microstructure of the treated materials (often metal alloys) on the propagation of the stress wave is negligible, both on the backface velocity, and on the induced residual stresses. This assumption can be used when the laser spots used (>1 mm) are several orders of magnitude larger than the average size of the grains of which the microstructures are composed, and therefore it completely neglects the heterogeneity of the residual stresses coming from the deformation heterogeneities in the microstructure. However, this "standard" configuration of LSP is not adapted to treat micro-components (for biomedical applications for example). In addition, the miniaturization of LSP, called micro-LSP, which makes use of femtosecond lasers and small laser spot sizes (Benxin et al., 2010) requires an enriched modeling because the use of macroscopic constitutive models (i.e. developed and identified on homogeneous macroscopic samples) is not relevant at such scales. Laser shock is also used to observe the dynamic behavior of materials using VISAR backface velocity measurements. Such results can be used to identify material constitutive behaviors (Ayad et al., 2022b,a; Seddik et al., 2022).

The problem to be considered is thus the one of the propagation of a stress wave in a polycrystalline microstructure. This situation has been mostly modeled in the literature in the case of *elastic* propagation, with an emphasis on acoustic, scattering and dispersion effects. For instance, Lan et al. (2014) report a dispersion on the wave velocity induced by random Zr microstructures, and other authors (Thompson et al., 2008; Ghoshal and Turner, 2009) investigate the attenuation of the wave, with notably Segurado and Lebensohn (2021) making use of a FFT approach. Plasticity during the shockwave propagation is also under consideration, either experimentally (see for example Winey et al. (2009) who interpret the differences of the wave attenuation in various Aluminum alloys as differences in plasticity mechanisms) or numerically, as in the work of Lloyd et al. (2014) who consider a 1D modeling of single and polycrystals and also highlight a dependence of the mechanical fields on the geometry of the microstructures. However, none of these approaches are consistently applied to LSP. Sunny et al. (2021) consider the simulation of a laser impact on a polycrystalline microstructure, but use a macroscopic Johnson-Cook model for the grains' plastic behavior, and Romanova et al. (2003) consider the propagation of a wave in a 3D polycrystalline microstructure but whose plastic behavior obeys a von Mises criterion. In the context of micro-LSP (laser spot diameter of a dozen μm), some authors consider the simulation of an impact on a single crystal in crystal plasticity (Chen et al., 2004; Zhang and Lawrence Yao, 2001; Wang et al., 2008; Chen et al., 2007), while others choose a purely experimental approach to the problem (Zhang et al., 2004). Only Vukelić et al. (2009) introduce simultaneously the formalism of crystal plasticity and material heterogeneity by modeling a bicrystal subjected to a laser shock. Additionally, the notion of dispersion of the mechanical field is discussed in the work of Case and Horie (2007), who study the propagation of a planar shock in a Copper polycrystal using discrete elements. Thus, the work on simulations of elastic–plastic stress wave propagation in a polycrystal in 2D or 3D is scarce (Clayton, 2005), especially in the case of LSP. The aim of this work is to investigate the effect of a polycrystalline microstructure on the elastic–plastic propagation of shockwave using crystal plasticity in order to investigate micro-LSP. Therefore this paper is concerned with the fundamental aspects of shockwave propagation in heterogeneous materials as well as applicative aspects since the problem considered is related to laser shock peening processing.

The article will be organized as follows. Section 2 is dedicated to the description of the modeling of the microstructures used, the elastic and plastic behaviors of the grains, and finally the stress wave equation in two dimensions. Following these first developments, Section 3 details the numerical treatment of the various aspects of the problems: the stress wave propagation, the crystal plasticity and the stress redistribution at the static equilibrium. Section 4 presents results on both a single crystal and on polycrystalline microstructures. A statistical approach is used to take into account the random nature of the microstructures. Finally, some aspects of the problems are discussed in Section 5, such as the influence on backface velocity profiles and the influence of the grain size.

2. Elastic–plastic stress waves in polycrystalline media

2.1. Problem considered

The objective of this section is to present the problem considered and the associated hypotheses. A 2D modeling is considered, as a compromise between a realistic modeling of the laser impact and reasonable computation times for the simulations. The situation to be modeled is represented in Fig. 1.

L_x and L_y are the dimensions of the spatial domain in the x and y directions respectively, and d is the diameter of the laser spot. We begin by recalling the equations describing the elastic behavior[1] of a material (in the absence of external forces):

$$\begin{cases} \text{div}\,(\sigma) = \rho(x,y)\dfrac{\partial^2 u}{\partial t^2} & \text{Dynamic equilibrium} \\[2mm] \sigma = \mathbb{C}(x,y):\varepsilon_e = \mathbb{C}(x,y):(\varepsilon - \varepsilon_p) & \text{Hooke's law} \\[2mm] \varepsilon(u) = \dfrac{1}{2}\left(\nabla u + \nabla^T u\right) & \text{Strain–displacement relation} \\[1mm] u(x,y,t=0) = \mathbf{0} & \text{Initial conditions,} \end{cases} \tag{1}$$

where σ is the stress tensor, ε the total strain tensor, ε_e the elastic strain tensor, ε_p the plastic strain tensor, and u the displacement field. The density is denoted ρ and the local stiffness tensor $\mathbb{C}(x,y)$. In order to eliminate the kinetic energy of the system to obtain a stationary plastic strain field, we will implement non-reflective boundary conditions to allow the stress wave to leave the domain. The implementation of these boundary conditions will be detailed in Section 4.1.

The two-dimensional modeling of the problem implies the choice of a modeling assumption: plane stresses (suitable for a very thin plate) or plane strains (suitable for a plate with infinite or very large thickness). In practical applications, neither of these two models corresponds to the standard experimental setup, requiring a 3D model. Nonetheless, a plane strain hypothesis is considered hereafter because it is closer to the experimental conditions than the plane stress hypothesis, and it will simplify the developments. Thus, the displacement field u can be expressed as follows:

$$u = u_x(x,y,t)e_1 + u_y(x,y,t)e_2. \tag{2}$$

In the following, the components of the displacement field (u_x and u_y), the deformation field (ε_{11}, ε_{22} and ε_{12}), and the stress fields (σ_{11}, σ_{22}, σ_{12} and σ_{33}) depend on the spatial and temporal coordinates, respectively x, y and t. The notations will however be dropped for the sake of clarity. The same is true for the dependence on the spatial coordinates of $\mathbb{C}$ and ρ. From Eq. $(1)_3$, it follows that the strain is of the form:

$$\varepsilon = \varepsilon_{11}e_1 \otimes e_1 + \varepsilon_{22}e_2 \otimes e_2 + \varepsilon_{12}(e_1 \otimes e_2 + e_2 \otimes e_1). \tag{3}$$

2.2. Geometrical modeling of a polycrystal

For the geometric representation of the polycrystalline microstructure, we consider a Poisson Voronoi Diagram (PVD) (Schneider et al., 2020). Thus, the probability that the number of grains in a microstructure is equal to a given value follows a Poisson distribution of parameter η, which corresponds to the average number of grains. Each grain is represented by a single point (called a seed). The seeds are uniformly distributed in the spatial domain, and grow isotropically, leading to isotropic microstructures. Illustrations are given in Figs. 8 and 17. It is possible for this Voronoi tesselation to identify the average grain size[2] (Zhang et al., 2012a,b).

Each grain can be assigned a different mechanical behavior. We consider that all the grains are identical in terms of mechanical properties (anisotropic $\mathbb{C}$ stiffness tensors in the crystal axes and uniform ρ densities), but not in terms of lattice orientations. In 3D, the crystalline orientation of a grain can be defined using Euler angles, denoted by φ_1, ϕ and φ_2 according to the Bunge convention (Bunge, 1982). For this 2D study, we keep $\phi = \varphi_2 = 0$, leading to the following rotation matrix $R(x,y)$:

$$R(x,y) = \begin{pmatrix} \cos\varphi_1(x,y) & -\sin\varphi_1(x,y) & 0 \\ \sin\varphi_1(x,y) & \cos\varphi_1(x,y) & 0 \\ 0 & 0 & 1 \end{pmatrix}. \tag{4}$$

---

[1] Only the elastic behavior is presented for the moment, the plastic behavior being the subject of a dedicated section.
[2] The grain size distribution obtained by a Voronoi diagram has a lower dispersion than a "real" microstructure (Lebensohn et al., 2005).

Table 1
Elasto-visco-plastic parameters for Aluminum AA1050 (Zhang et al., 2015).

C_{1111} (GPa)	C_{1122} (GPa)	C_{1212} (GPa)	$\dot{\gamma}_0$ (s^{-1})	$1/m$	g_0 (MPa)
106.75	60.41	28.34	0.001	16	12.9

2.3. Elastic behavior

We consider a cubic elastic symmetry, represented by the stiffness tensor $\mathbb{C}^0$ in the reference frame associated with the crystal lattice is solely described by the coefficients C_{1111}^0, C_{1122}^0 and C_{1212}^0, with $2C_{1212}^0(x, y) \neq C_{1111}^0(x, y) - C_{1122}^0(x, y)$. As indicated in Section 2.2, each grain in the Voronoi tessellation will have a different crystal orientation. The stiffness tensor expressed in the sample reference frame, noted $\mathbb{C}(x, y)$, is given by (assuming the Einstein notation for the implicit summation of repeated indexes):

$$\mathbb{C}_{ijkl} = R_{im} R_{jn} R_{ko} R_{lp} \mathbb{C}_{mnop}^0. \tag{5}$$

As an example, considering an Aluminum-type behavior (Zhang et al., 2015)($C_{1111} = 106.75$ GPa, $C_{1122} = 60.41$ GPa, $C_{1212} = 28.34$ GPa, see Table 1), variations of φ_1 can induce maximal variations of approximately 5% increase on C_{1111}, a 10% decrease on C_{1122} and a 20% decrease on C_{1212}. They also induce non zero C_{1112} and C_{2212} which are otherwise null in the crystal frame of reference. The rest of the C_{ijkl} components remain equal to 0. It should be noted that an elasticity tensor with a cubic symmetry and variations of φ_1 only do not lead to out of plane strain or stress components.

2.4. Plastic behavior

Plasticity at the crystal scale stems from dislocation movements on slip systems. Crystal plasticity models introduce internal variables corresponding to plastic multipliers $\gamma^{(\alpha)}$ specific to each slip system. The plastic strain rate is given by:

$$\dot{\varepsilon}_p = \sum_\alpha \dot{\gamma}^{(\alpha)} \mu^{(\alpha)}, \tag{6}$$

where $\mu^{(\alpha)}$ is the symmetric Schmid tensor of the α slip system, defined as:

$$\mu^{(\alpha)} = \frac{1}{2} \left(t^{(\alpha)} \otimes n^{(\alpha)} + n^{(\alpha)} \otimes t^{(\alpha)} \right), \tag{7}$$

with $t^{(\alpha)}$ and $n^{(\alpha)}$ unit vectors parallel to the direction and normal of the slip system, respectively. It is also possible to compute the elastic rotation of the crystal lattice, defined as:

$$\dot{\omega} = \dot{\omega}_e + \dot{\omega}_p, \tag{8}$$

where $\dot{\omega}_p$ is the plastic rotation rate given by:

$$\dot{\omega}_p = \sum_\alpha \dot{\gamma}^{(\alpha)} \mu_{skew}^{(\alpha)}, \tag{9}$$

where $\mu_{skew}^{(\alpha)}$ are the skew-symmetric Schmid tensors:

$$\mu_{skew}^{(\alpha)} = \frac{1}{2} \left(t^{(\alpha)} \otimes n^{(\alpha)} - n^{(\alpha)} \otimes t^{(\alpha)} \right). \tag{10}$$

Finally, $\dot{\omega}$ is the total rotation rate, which is the skew-symmetric part of the velocity gradient:

$$\dot{\omega} = \frac{1}{2} \left(\nabla v - \nabla^T v \right). \tag{11}$$

As presented in Section 2.1, we wish to guarantee a plane strain state during the propagation of the stress wave, and therefore we consider only two slip systems, arbitrarily fixed and expressed in the crystal frame by:

$$\begin{cases} n^{(1)} = (1, 0, 0) \\ t^{(1)} = (0, 1, 0) \end{cases} \quad \begin{cases} n^{(2)} = \dfrac{1}{\sqrt{2}}(1, 1, 0) \\ t^{(2)} = \dfrac{1}{\sqrt{2}}(-1, 1, 0). \end{cases} \tag{12}$$

The slip system 2 corresponds to the slip system 1 rotated by 45°. The slip plane normal and slip directions were chosen parallel to the x–y plane to avoid any out-of-plane plastic strain, so as to stay with a 2D problem. These two slip systems were chosen in order to (i) speed up the numerical computation (the numerical cost increases with the number of slip systems, see Section 3.2) and (ii) to deal with a plastic behavior exhibiting an anisotropy somehow similar to standard metallic alloys (more slip systems would have reduced the plastic anisotropy, and only one slip systems would have increased it tremendously). We can then verify that the symmetric Schmid tensors in the crystal reference frame do not generate any out-of-plane plastic strain:

$$\mu_0^{(1)} = \frac{1}{2} \begin{pmatrix} 0 & 1 & 0 \\ 1 & 0 & 0 \\ 0 & 0 & 0 \end{pmatrix} \quad \text{and} \quad \mu_0^{(2)} = \frac{1}{2} \begin{pmatrix} -1 & 0 & 0 \\ 0 & 1 & 0 \\ 0 & 0 & 0 \end{pmatrix}. \tag{13}$$

From the form of the symmetric Schmid tensors given in Eq. (13), the plastic strain tensor has the following general form:

$$\boldsymbol{\varepsilon}_p = \begin{pmatrix} \varepsilon_p & \varepsilon_{p,12} & 0 \\ \varepsilon_{p,12} & -\varepsilon_p & 0 \\ 0 & 0 & 0 \end{pmatrix}, \tag{14}$$

and the skew-symmetric Schmid tensors are

$$\boldsymbol{\mu}_{skew,0}^{(1)} = \boldsymbol{\mu}_{skew,0}^{(2)} = \frac{1}{2}\begin{pmatrix} 0 & -1 & 0 \\ 1 & 0 & 0 \\ 0 & 0 & 0 \end{pmatrix}. \tag{15}$$

Schmid tensors can also be expressed in the sample frame:

$$\boldsymbol{\mu}_{ij}(x, y) = \boldsymbol{R}_{im}(x, y)\boldsymbol{R}_{jn}(x, y)\boldsymbol{\mu}_{0mn}. \tag{16}$$

The skew-symmetric Schmid tensors are invariant by any rotation of φ_1. The influence of the crystal orientation on the plastic rotation will therefore come from the values of $\dot{\gamma}^{(\alpha)}$ only, unlike plastic strain, which is influenced by crystal orientation. The chosen slip systems thus contribute to preserving the plane strain nature of the problem, both through the plastic strain and plastic rotation tensors. For example, this is not possible if the coordinates of the normal and direction of a slip system have a component along e_3.

The computation of the shear rate $\dot{\gamma}^{(\alpha)}$ is done using the visco-plastic constitutive relation developed by Hutchinson (1976) in which the plastic multipliers of the slip planes are given by:

$$\dot{\gamma}^{(\alpha)} = \dot{\gamma}_0 \frac{\tau^{(\alpha)}}{g^{(\alpha)}} \left| \frac{\tau^{(\alpha)}}{g^{(\alpha)}} \right|^{\frac{1}{m}-1} = \dot{\gamma}_0^{(\alpha)} \text{sign}\left(\frac{\tau^{(\alpha)}}{g^{(\alpha)}} \right) \left| \frac{\tau^{(\alpha)}}{g^{(\alpha)}} \right|^{\frac{1}{m}}, \tag{17}$$

where $\dot{\gamma}_0$ is a parameter representing a reference strain-rate, and m is a positive exponent, controlling the strain-rate sensitivity. The resolved shear stress on the α slip system $\tau^{(\alpha)}$ is given by $\tau^{(\alpha)} = \boldsymbol{\sigma} : \boldsymbol{\mu}^{(\alpha)}$. Finally, $g^{(\alpha)}$ is the yield strength of the slip system α. In this work, we will use a modified formulation of Eq. (17), introducing threshold model (another example can be found in Méric et al. (1994)):

$$\begin{cases} \dot{\gamma}^{(\alpha)} = 0 & \text{if } \left| \tau^{(\alpha)} \right| \le g^{(\alpha)} \\ \dot{\gamma}^{(\alpha)} = \dot{\gamma}_0 \frac{\tau^{(\alpha)}}{g^{(\alpha)}} \left| \frac{\tau^{(\alpha)}}{g^{(\alpha)}} \right|^{\frac{1}{m}-1} & \text{if } \left| \tau^{(\alpha)} \right| > g^{(\alpha)}. \end{cases} \tag{18}$$

This formulation allows the optimization of the numerical resolution of the visco-plastic model, since plasticity is induced only if the resolved shear stress on a slip system is higher than the associated critical shear stress. The equations are therefore not solved at any point of the spatial domain, but only at those requiring a plastic correction.

2.5. Elastic–plastic wave in two dimensions

Hooke's law (1)$_2$ with $\mathbb{C}$ introduced Section 2.3 together with the plane strain assumption thus gives:

$$\boldsymbol{\sigma} = \sigma_{11}e_1 \otimes e_1 + \sigma_{22}e_2 \otimes e_2 + \sigma_{33}e_3 \otimes e_3 + \sigma_{12}(e_1 \otimes e_2 + e_2 \otimes e_1). \tag{19}$$

With the assumption of plane strains, the stress component σ_{33} can be obtained from the components σ_{11}, σ_{22} and σ_{12} via Hooke's law. To obtain the propagation equation, we follow the methodology of Leveque (2002). The dynamic equilibrium Eq. (1)$_1$ leads to the following system:

$$\begin{cases} \dfrac{\partial \sigma_{11}}{\partial x} + \dfrac{\partial \sigma_{12}}{\partial y} = \rho(x, y)\dfrac{\partial v_x}{\partial t} \\ \dfrac{\partial \sigma_{12}}{\partial x} + \dfrac{\partial \sigma_{22}}{\partial y} = \rho(x, y)\dfrac{\partial v_y}{\partial t}, \end{cases} \tag{20}$$

where v_x and v_y are the components of the material velocity field $\boldsymbol{v}$, such that $v_x = \partial u_x/\partial t$ and $v_y = \partial u_y/\partial t$. Moreover, with the assumption of small perturbations, we have

$$\begin{cases} \dfrac{\partial \varepsilon_{11}}{\partial t} = \dfrac{\partial}{\partial t}\left(\dfrac{\partial u_x}{\partial x} \right) = \dfrac{\partial}{\partial x}\left(\dfrac{\partial u_x}{\partial t} \right) = \dfrac{\partial v_x}{\partial x} \\ \dfrac{\partial \varepsilon_{22}}{\partial t} = \dfrac{\partial}{\partial t}\left(\dfrac{\partial u_y}{\partial y} \right) = \dfrac{\partial}{\partial y}\left(\dfrac{\partial u_y}{\partial t} \right) = \dfrac{\partial v_y}{\partial y} \\ \dfrac{\partial \varepsilon_{12}}{\partial t} = \dfrac{1}{2}\dfrac{\partial}{\partial t}\left(\dfrac{\partial u_x}{\partial y} + \dfrac{\partial u_y}{\partial x} \right) = \dfrac{1}{2}\left(\dfrac{\partial v_x}{\partial y} + \dfrac{\partial v_y}{\partial x} \right). \end{cases} \tag{21}$$

Hooke's law (1)$_1$ derived with respect to time gives:

$$\begin{cases} \dfrac{\partial \sigma_{11}}{\partial t} = C_{1111}\left(\dfrac{\partial v_x}{\partial x} - \dfrac{\partial \varepsilon_p}{\partial t} \right) + C_{1122}\left(\dfrac{\partial v_y}{\partial y} + \dfrac{\partial \varepsilon_p}{\partial t} \right) + C_{1112}\left(\dfrac{\partial v_x}{\partial y} + \dfrac{\partial v_y}{\partial x} - 2\dfrac{\partial \varepsilon_{p,12}}{\partial t} \right) \\ \dfrac{\partial \sigma_{22}}{\partial t} = C_{1122}\left(\dfrac{\partial v_x}{\partial x} - \dfrac{\partial \varepsilon_p}{\partial t} \right) + C_{2222}\left(\dfrac{\partial v_y}{\partial y} + \dfrac{\partial \varepsilon_p}{\partial t} \right) + C_{2212}\left(\dfrac{\partial v_x}{\partial y} + \dfrac{\partial v_y}{\partial x} - 2\dfrac{\partial \varepsilon_{p,12}}{\partial t} \right) \\ \dfrac{\partial \sigma_{12}}{\partial t} = C_{1112}\left(\dfrac{\partial v_x}{\partial x} - \dfrac{\partial \varepsilon_p}{\partial t} \right) + C_{2212}\left(\dfrac{\partial v_y}{\partial y} + \dfrac{\partial \varepsilon_p}{\partial t} \right) + C_{1212}\left(\dfrac{\partial v_x}{\partial y} + \dfrac{\partial v_y}{\partial x} - 2\dfrac{\partial \varepsilon_{p,12}}{\partial t} \right). \end{cases} \tag{22}$$

For the resolution of the stress wave equation, we will assume a purely elastic propagation, i.e. $\partial \varepsilon_p / \partial t = \partial \varepsilon_{p,12} / \partial t = 0$. This step will act as an elastic predictor step, after which a plastic correction will be made, as addressed in Section 3.2. More precisely, a plastic strain increment $\Delta \varepsilon_p$ is computed using the crystal plasticity visco-plastic constitutive behavior, which is then used to correct with Hooke's law the stress initially obtain by solving the stress wave propagation. An alternative would be to compute tangent moduli corresponding to the correct level of plastic strain and use it to derive an alternative version of the stress wave equation (see for instance Lapostolle et al., 2022a). However, because of the crystal plasticity model used, finding these moduli *at each iteration and at each node* can be very computationally demanding. It has been shown in a homogeneous macroscopic 1D case that both approaches lead to very similar results (see Appendix A of Lapostolle, 2022) The systems (20) and (22) can be grouped into the following matrix equation, using the notations of Leveque (2002):

$$\frac{\partial U}{\partial t} + A(x,y)\frac{\partial U}{\partial x} + B(x,y)\frac{\partial U}{\partial y} = 0,$$ (23)

where U is the vector of unknowns such that $U = (\sigma_{11}, \sigma_{22}, \sigma_{12}, v_x, v_y)^T$. The matrices A and B are constructed such that:

$$A(x,y) = \begin{pmatrix} 0 & 0 & 0 & -C_{1111} & -C_{1112} \\ 0 & 0 & 0 & -C_{1122} & -C_{2212} \\ 0 & 0 & 0 & -C_{1112} & -C_{1212} \\ -\frac{1}{\rho} & 0 & 0 & 0 & 0 \\ 0 & 0 & -\frac{1}{\rho} & 0 & 0 \end{pmatrix}, \quad B(x,y) = \begin{pmatrix} 0 & 0 & 0 & -C_{1112} & -C_{1122} \\ 0 & 0 & 0 & -C_{2212} & -C_{2222} \\ 0 & 0 & 0 & -C_{1212} & -C_{2212} \\ 0 & 0 & -\frac{1}{\rho} & 0 & 0 \\ 0 & -\frac{1}{\rho} & 0 & 0 & 0 \end{pmatrix}.$$ (24)

Eq. (23) corresponds to the advection equation in two dimensions, and models here the propagation of a stress wave in plane strains, including three wave propagation phenomena: a longitudinal tension/compression wave (in the direction of impact), a transverse tension/compression wave (perpendicular to the direction of impact), and a shear wave (the velocity of the latter differs according to longitudinal or transverse directions). With the numerical values of C_{ijkl} indicated in Section 2.3, the change of the wave velocities in the principal directions caused by the change of crystal orientation is approximately of 2.5% increase, and of 10% decrease for the shear waves.

3. Numerical methods

3.1. Numerical scheme for the stress wave propagation in two dimensions

Let U_{ij}^n be the vector of discretized unknowns, evaluated at time increment n and spatial cell ij, corresponding to the point with coordinates (x_i, y_j). The coordinates x_i and y_j correspond to the spatial discretization defined as $x_{i+1} = x_i + \Delta x$ and $y_{j+1} = y_j + \Delta y$. We also introduce the time increment Δt such that $t^{n+1} = t^n + \Delta t$. In order to solve numerically Eq. (23), we will use an explicit numerical integration scheme. This type of algorithm produces stable results only if it verifies the so-called CFL (Courant–Friedrichs–Lewy) condition defined as:

$$\text{CFL} = c_{\max}\frac{\Delta t}{\Delta x} \leq 1,$$ (25)

where

$$c_{\max} = \max_{x,y \in [0,L_x] \times [0,L_y]} \left\{ c_{\text{longi}}(x,y), c_{\text{trans}}(x,y), c_{\text{shear}}(x,y) \right\},$$ (26)

where c_{longi}, c_{trans} and c_{shear} are the longitudinal, transversal and shear wave velocities respectively (here $c_{\text{longi}} = c_{\text{trans}}$ since $C_{1111} = C_{2222}$). In fact, $c_{\max}$ is imposed by the material's behavior, and CFL and Δx are input data to the simulations, with which it is possible to determine the value of Δt using Eq. (25). According to Leveque (2002), the general form of the numerical solution of Eq. (23) takes here the following form:

$$U_{i,j}^{n+1} = U_{i,j}^n - \frac{\Delta t}{\Delta x}\left(F_{i+1/2,j}^n - F_{i-1/2,j}^n\right) - \frac{\Delta t}{\Delta y}\left(G_{i,j+1/2}^n - G_{i,j-1/2}^n\right),$$ (27)

where the $F_{i+1/2,j}^n$, $F_{i-1/2,j}^n$, $G_{i,j+1/2}^n$ and $G_{i,j-1/2}^n$ are denoted as fluxes, and whose expression varies depending on the numerical method. In addition to the usual considerations on the ability of the numerical method to introduce few numerical errors, it becomes necessary in the 2D case to optimize the resolution in order to limit the computation time. For these reasons, the Godunov method, suitable for hyperbolic systems (Leveque, 2002; Lapostolle et al., 2022b) is used here. For the sake of conciseness, the details of this method are provided in Appendix A. An improvement of the numerical method is also possible, by using the Godunov High Resolution method (see for instance Lapostolle et al., 2022a; Heuzé, 2017). This last method is however non linear, as it involves a corrective term based on a flux limiter, and its implementation yields significantly longer computation times in the case of elasto-visco-plastic behavior.

3.2. Treatment of crystal plasticity

When solving numerically a crystal plasticity problem, the system has as many internal variables as slip systems. Indeed, the knowledge of the plastic multipliers makes it possible to deduce the rest of the variables of the problem, from the deformation to the stress, along with the rotation of the crystal lattice. The first order time derivatives are here discretized by a forward Euler scheme. Using the methodology of Huang (1991) (see also Harewood and McHugh, 2007), the plastic multipliers increments $\Delta\gamma^{(\alpha)}$ can be expressed as follows:

$$\Delta\gamma^{(\alpha)} = (1 - \theta)\,\Delta t \dot{\gamma}^{(\alpha),n} + \theta\,\Delta t \dot{\gamma}^{(\alpha),n+1}. \tag{28}$$

They are thus determined by linear interpolation (controlled by a parameter θ such that $\theta \in [0, 1]$) of the temporal variations of $\dot{\gamma}^{(\alpha)}$ at the previous time $\dot{\gamma}^{(\alpha),n}$ and at the next time $\dot{\gamma}^{(\alpha),n+1}$. Using Eq. (17), we thus obtain:

$$\Delta\gamma^{(\alpha)} = (1 - \theta)\,\Delta t \dot{\gamma}^{(\alpha),n} + \theta\,\Delta t \dot{\gamma}_0 \frac{\tau^{(\alpha),n+1}}{g^{(\alpha)}} \left| \frac{\tau^{(\alpha),n+1}}{g^{(\alpha)}} \right|^{\frac{1}{m}-1}, \tag{29}$$

with

$$\tau^{(\alpha),n+1} = \sigma^{n+1} : \mu^{(\alpha)} = (\sigma^n + \Delta\sigma) : \mu^{(\alpha)} = \tau^{(\alpha),n} + \Delta\tau^{(\alpha)}, \tag{30}$$

where $\tau^{(\alpha),n}$ is the resolved shear stress of the α system at the time step n and $\Delta\tau^{(\alpha)}$ is the resolved shear stress increment, computed by:

$$\Delta\tau^{(\alpha)} = \Delta\sigma : \mu^{(\alpha)} = \mathbb{C} : \left(\Delta\varepsilon - \Delta\varepsilon_p\right) : \mu^{(\alpha)} = \Delta\sigma_{\text{el}} : \mu^{(\alpha)} - \mathbb{C} : \Delta\varepsilon_p : \mu^{(\alpha)}. \tag{31}$$

$\Delta\sigma_{\text{el}}$ corresponds to the stress increment resulting from the elastic propagation calculation, before a possible plastic correction step takes place. Using Eq. (6), Eq. (29) thus becomes:

$$\Delta\gamma^{(\alpha)} - (1-\theta)\Delta t\dot{\gamma}^{(\alpha),n} - \frac{\theta\,\Delta t\dot{\gamma}_0}{g^{(\alpha)}} \left(\tau^{(\alpha),n} + \Delta\sigma_{\text{el}} : \mu^{(\alpha)} - \mathbb{C} : \sum_\beta \mu^{(\beta)} \Delta\gamma^{(\beta)} : \mu^{(\alpha)} \right) \times$$
$$\left| \tau^{(\alpha),n} + \Delta\sigma_{\text{el}} : \mu^{(\alpha)} - \mathbb{C} : \sum_\beta \mu^{(\beta)} \Delta\gamma^{(\beta)} : \mu^{(\alpha)} \right|^{\frac{1}{m}-1} = 0. \tag{32}$$

Finally, in the present case where we consider only two slip systems without hardening ($g^{(\alpha)} = g_0$), the system to solve is:

$$\begin{cases} \Delta\gamma^{(1)} - (1 - \theta)\Delta t\dot{\gamma}^{(1),n} - \dfrac{\theta\,\Delta t\dot{\gamma}_0}{g_0} \left(\tau^{(1),n} + \Delta\sigma_{\text{el}} : \mu^{(1)} - \mathbb{C} : \left(\mu^{(1)}\Delta\gamma^{(1)} + \mu^{(2)}\Delta\gamma^{(2)}\right) : \mu^{(1)} \right) \times \\ \left| \tau^{(1),n} + \Delta\sigma_{\text{el}} : \mu^{(1)} - \mathbb{C} : \left(\mu^{(1)}\Delta\gamma^{(1)} + \mu^{(2)}\Delta\gamma^{(2)}\right) : \mu^{(1)} \right|^{\frac{1}{m}-1} = 0 \\ \Delta\gamma^{(2)} - (1 - \theta)\Delta t\dot{\gamma}^{(2),n} - \dfrac{\theta\,\Delta t\dot{\gamma}_0}{g_0} \left(\tau^{(2),n} + \Delta\sigma_{\text{el}} : \mu^{(2)} - \mathbb{C} : \left(\mu^{(1)}\Delta\gamma^{(1)} + \mu^{(2)}\Delta\gamma^{(2)}\right) : \mu^{(2)} \right) \times \\ \left| \tau^{(2),n} + \Delta\sigma_{\text{el}} : \mu^{(2)} - \mathbb{C} : \left(\mu^{(1)}\Delta\gamma^{(1)} + \mu^{(2)}\Delta\gamma^{(2)}\right) : \mu^{(2)} \right|^{\frac{1}{m}-1} = 0 \end{cases} \tag{33}$$

This equation, which has as many unknowns as plastic multipliers, is solved using a multi-dimensional Newton method. Once the $\Delta\gamma^{(\alpha)}$ are determined, it is then possible to compute the plastic strain using Eq. (6), the plastic rotation of the crystal lattice using Eq. (9), and the new stress state using Hooke's law. In our case, it has been observed that the numerical parameter θ has only a limited influence on the results for $0.5 \leq \theta \leq 1$. We will take $\theta = 1$ in the following, making the resolution completely implicit.

The final stress state σ^{n+1} is calculated as follows:

$$\sigma^{n+1} = \sigma_{\text{el}}^{n+1} - \mathbb{C} : \Delta\varepsilon_p, \tag{34}$$

where σ_{el}^{n+1} is the stress state computed in a purely elastic way with Eq. (27).

In summary, at each time step, an elastic predictor step is computed by solving Eq. (23) using Eq. (27). The criterion of Eq. (18) is then checked, and a correction is applied if needed using Eqs. (33), (6) and (34).

3.3. Numerical scheme for the stress redistribution

The objective of this section is to detail the computation of the *residual stress field*. The residual stresses correspond to a non-zero stress state present in the material even though all external loading has disappeared. However, the residual stresses are non-zero if and only if the plastic strains are non-uniform, i.e. if they present a gradient. The problem is represented schematically in Fig. 2.
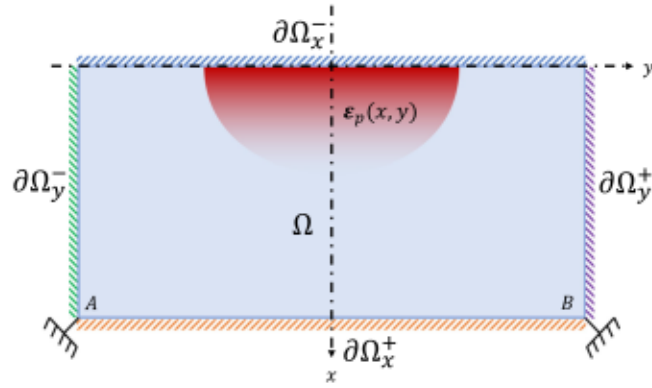
Fig. 2. Representation of the problem for the determination of residual stresses.

The heterogeneous field of residual plastic strains induced by the laser shock responsible for the residual stresses is shown in Fig. 2. The determination of the residual stresses consists in finding the displacement field $u(x, y)$ such that:

$$
\begin{cases}
\text{div}(\sigma) = 0 \\
\sigma = \mathbb{C}(x, y) : (\varepsilon(x, y) - \varepsilon_p(x, y)) \\
\varepsilon = \frac{1}{2}(\nabla u + \nabla^T u). \\
\sigma.n = 0 \quad \text{on} \quad \partial\Omega_x^- \cup \partial\Omega_x^+ \cup \partial\Omega_y^- \cup \partial\Omega_y^+ = \partial\Omega \\
u = 0 \quad \text{at A and B.}
\end{cases}
\tag{35}
$$

In Eq. (35), the plastic strain tensor $\varepsilon_p(x, y)$ comes from the elasto-plastic propagation step (Sections 3.1 and 3.2), and is therefore an input, as well as the stiffness tensor field $\mathbb{C}(x, y)$. Another possibility would be to run the propagation simulation for a longer period of time ($\sim$10 µs) in order to eventually obtain a static equilibrium. This however is more computationally demanding than the proposed method. The only requirement here is that the plastic strain field has become stationary, even though the stress wave may still be propagating. The displacement field keeps the form of Eq. (2), without the time dependency.

As shown in Fig. 2, the surfaces of the sample will be considered as free surfaces, and clamps are imposed at points A and B. Thus:

$$
\begin{cases}
\text{On } \partial\Omega_x^- \text{ and } \partial\Omega_x^+ : \begin{cases} \sigma_{11}(x, y) = 0 \\ \sigma_{12}(x, y) = 0 \end{cases} \\
\text{On } \partial\Omega_y^- \text{ and } \partial\Omega_y^+ : \begin{cases} \sigma_{22}(x, y) = 0 \\ \sigma_{12}(x, y) = 0 \end{cases} \\
\text{At } A \text{ and } B : \quad u_x = u_y = 0
\end{cases}
\tag{36}
$$

The heterogeneity of the stiffness tensor field must also be taken into account in the resolution, which leads:

$$
\sigma_{ij/q} = C_{ijkl/q} (\varepsilon_{kl} - \varepsilon_{p,kl}) + C_{ijkl} (\varepsilon_{kl/q} - \varepsilon_{p,kl/q}),
\tag{37}
$$

where the notation $./q$ corresponds to the partial derivative with respect to the q coordinate, here x or y. Here, the spatial distributions of C_{ijkl} quantities will be assumed constant per grain, with jumps at the interfaces. The considered finite difference implementation, in which the spatial increments are constant throughout the spatial domain, does not allow a mesh refinement at the interfaces. These quantities are therefore not strictly derivable at the grain boundaries and the derivatives are therefore to be considered only in the numerical sense.

The resolution of the system (35) involves the first and second spatial derivatives of the displacement field, expressed using a finite difference scheme. The expression of the static equilibrium (35) (see Appendix B for more details) can be cast in the following form:

$$
MX = f \iff \begin{pmatrix} M_{11} & M_{12} \\ M_{21} & M_{22} \end{pmatrix} \begin{pmatrix} U_x \\ U_y \end{pmatrix} = \begin{pmatrix} f_1 \\ f_2 \end{pmatrix},
\tag{38}
$$

with $U_x = \left(u_{x,11}\ u_{x,12} \cdots u_{x,1N_y}\ u_{x,21} \cdots u_{x,ij} \cdots u_{x,N_x1} \cdots u_{x,N_xN_y} \right)^T$ and U_y defined in a similar way. The matrices M_{IJ} for $I, J \in \{1, 2\} \times \{1, 2\}$ are constructed with the parameters Δx, Δy and the coefficients C_{klmn}. The vectors f_1 and f_2 are also constructed with Δx, Δy, C_{klmn} but also the values of the components of the plastic strain tensor evaluated at a given node $\varepsilon_{p,ij}$. The construction of matrix M and vector f of Eq. (38) is presented in Appendix B. The boundary conditions in Eq. (36) are incorporated into the system of Eq. (38) at the corresponding lines. The inversion of matrix M then leads to the solution of the problem.
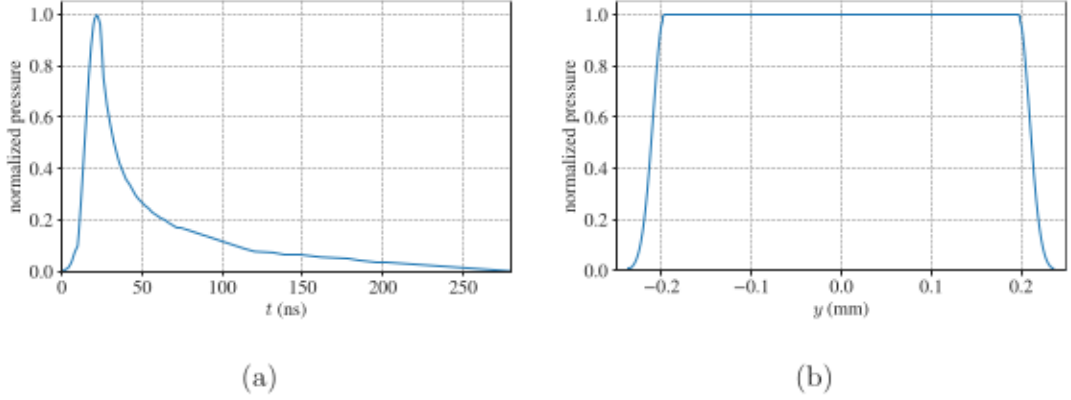
Fig. 3. Modeling of the pressure loading from the laser impact. The pressure is normalized. (a) Temporal profile. (b) Spatial profile.

4. Numerical results

4.1. Numerical simulation of elastic–plastic laser shock wave in single crystals

We first consider the case of a single crystal, which will allow us to assess the influence of the crystal orientation on the plastic residual strain field after a laser shock.

Simulation parameters. We consider a rectangular domain of physical dimensions $L_x = L_y = 3$ mm. The numbers of nodes in the x and y directions, noted N_x and N_y respectively, are $N_x = N_y = 600$.

The laser loading is modeled by a typical spatial and temporal pressure profiles which are taken from the work of Le Bras et al. (2019) and illustrated with a normalized pressure in Fig. 3. This pressure is applied as a boundary condition on the Ω_x^- boundary (see Fig. 2). The diameter d of the laser spot is fixed at $d = 0.5$ mm, in order to approximate the experimental conditions of LSP. It should be noted that the spatial profile shown in Fig. 3(b) is idealized for this laser size diameter, the profile being much more heterogeneous in experimental measurements. Moreover, the pressure amplitude will be $P = 1$ GPa.

The material parameters used are close to those of Aluminum AA1050[3] (Zhang et al., 2015), see Table 1.

The computation of the residual stresses is based on the residual plastic strain field. This field will be generated in our case by a single laser impact. Since the calculation of residual stresses generally corresponds to a thick sample, it is necessary to ensure that the plastic strains are not modified by wave reflections caused by the edges of the numerical domain. For this purpose, we use non-reflective (or outflow) boundary conditions in the calculation of the elasto-plastic propagation, allowing the stress wave to leave the spatial domain of the simulation as if it were propagating at infinity. These boundary conditions correspond to a zero-order extrapolation of the unknowns at the domain boundaries (see Fig. 2) (Leveque, 2002):

$$\begin{cases} \text{On } \partial\Omega_x^+ : \ \boldsymbol{U}_{N_x j} = \boldsymbol{U}_{N_x-1 j} \\ \text{On } \partial\Omega_y^- : \ \boldsymbol{U}_{i0} = \boldsymbol{U}_{i1} \\ \text{On } \partial\Omega_y^+ : \ \boldsymbol{U}_{iN_y} = \boldsymbol{U}_{iN_y-1}. \end{cases} \qquad (39)$$

These boundary conditions mean that on the concerned boundaries, the row (on $\partial\Omega_x^+$) and columns (on $\partial\Omega_y^-$ and $\partial\Omega_y^+$) of the grid will be attributed the values of the closest row and columns respectively, which are computed using the numerical scheme. The unknowns of row N_x take the value of row $N_x - 1$ ($\forall j$), the unknowns of column 0 take the values of column 1, and the unknowns of column N_y take the value of column $N_y - 1$ ($\forall i$).

Plastic strain field. We begin by presenting the results in terms of the accumulated plastic strain γ, defined as

$$\gamma = \sum_\alpha \left| \gamma^{(\alpha)} \right|, \qquad (40)$$

whose distributions are presented in Fig. 4 for two sample orientations, $\varphi_1 = 0$ and $\varphi_1 = \pi/6$, in order to illustrate how the orientation of a single crystal can influence the results. To these results are added lines representing the slip directions of the slip systems, to make the interpretation clearer. The orientation of these lines has not been fitted from the maps in Fig. 4, but has been drawn so as to respect the angles of the slip systems with the e_1 direction.

Fig. 4 shows that the orientation of the crystal with respect to the impact direction has a strong influence on the plastic strain distribution, but a limited influence on its values. Figs. 4(a) and 4(b) both show areas of high plastic strain at the edges of the

---

[3] The behavior of Aluminum is used for the material elastic constants, but not for the geometry of the microstructure, nor for the slip systems used in the visco-plastic behavior.
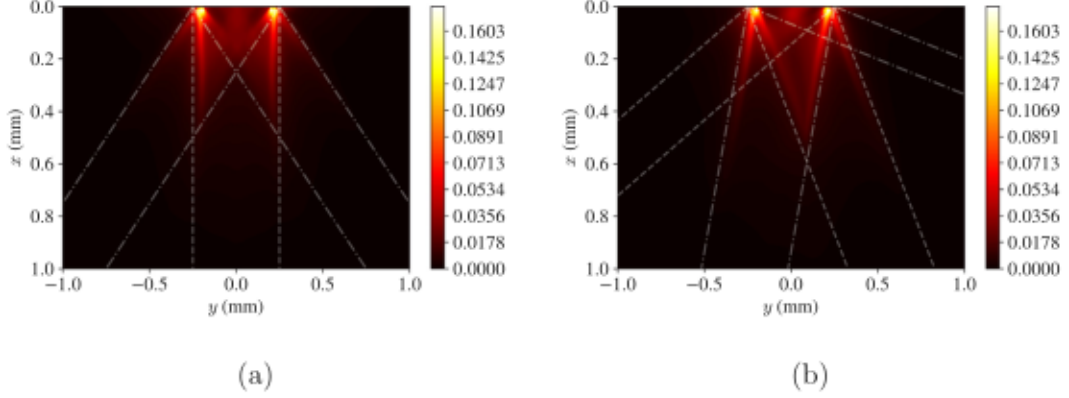
Fig. 4. Accumulated plastic strain γ (enlarged visual) for a single impact on a single crystal. White dashed lines correspond to slip directions of slip system 1, and white dashed/dotted lines correspond to slip directions of slip system 2. (a) Crystal orientation defined by $\varphi_1 = 0$. (b) Crystal orientation defined by $\varphi_1 = \pi/6$.
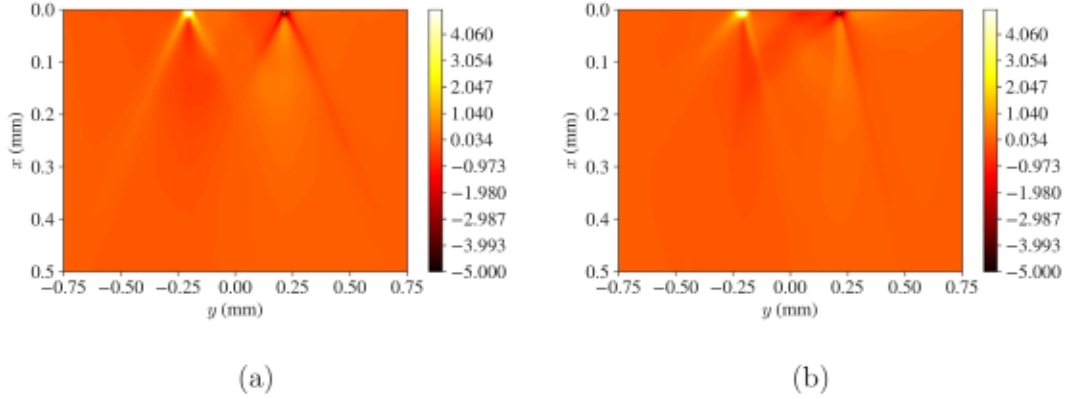
Fig. 5. Elastic rotations of the crystal lattice in degree (enlarged visual) for a single impact on a single crystal. (a) Orientation of the crystal defined by $\varphi_1 = 0$. (b) Crystal orientation defined by $\varphi_1 = \pi/6$.

impact, which is due to shear between the compressed area of the impact and the free area. It is interesting to note that each figure shows localization bands of plastic strain originating from the edges of the impact. The pattern formed by these lines is different between the orientation $\varphi_1 = 0$ (where it is symmetrical with respect to $y = 0$) and $\varphi_1 = \pi/6$ (where it is not symmetrical). These lines can be interpreted as the directions of the slip systems, which are activated by high values of resolved shear stress. This is why they originate from the edges of the impact, where a shear stress is found with respect to the center of the impact (the latter being in a state close to pure compression, whereas shear is added at the edges of the laser spot). It is important to note that a slip system in a reference position and rotated by 90° generates the same amount of plastic strain in absolute value, as

$$\left| \boldsymbol{\sigma} : \boldsymbol{\mu}^{(\alpha)} \right| = \left| \boldsymbol{\sigma} : \boldsymbol{R}_{90} \cdot \boldsymbol{\mu}^{(\alpha)} \cdot \boldsymbol{R}_{90}^T \right|, \tag{41}$$

where $\boldsymbol{R}_{90}$ is the rotation matrix for $\varphi_1 = 90°$. This is why each slip system gives rise to two localization bands, one parallel to $t^{(\alpha)}$, and another perpendicular to it. It is also interesting to study the results for the rotation of the crystal lattice induced by the laser shock. Indeed, this rotation is a marker of the plastic strain. Fig. 5 presents the elastic rotation ω_e maps, in degrees, for the orientations $\varphi_1 = 0$ and $\varphi_1 = \pi/6$.

LSP leads to lattice rotation of a few degrees, localized in similar bands as the accumulated plastic strain. The rotations are however zero in the center of the impact, indicating that the matter is compressed uniformly in this region.

Residual stress field. We present in Fig. 6 the residual stresses induced by the plastic strain field.

We can notice that the residual stress distribution in the single crystal for both orientations also follows the slip lines highlighted in Fig. 4. Both maps in Fig. 6 show stress concentrations at the edges of the impact, where the shear strain is maximum. Before being able to draw conclusions on the influence of a microstructure on the residual stresses, the distribution of the latter is already impacted by the orientation of the grains. This influence is observed in more detail in Fig. 7, where the spatial profiles of the residual stresses as a function of the depth at the center of the impact ($y = 0$) are presented. These stress profiles for angles $\varphi_1 = 0$
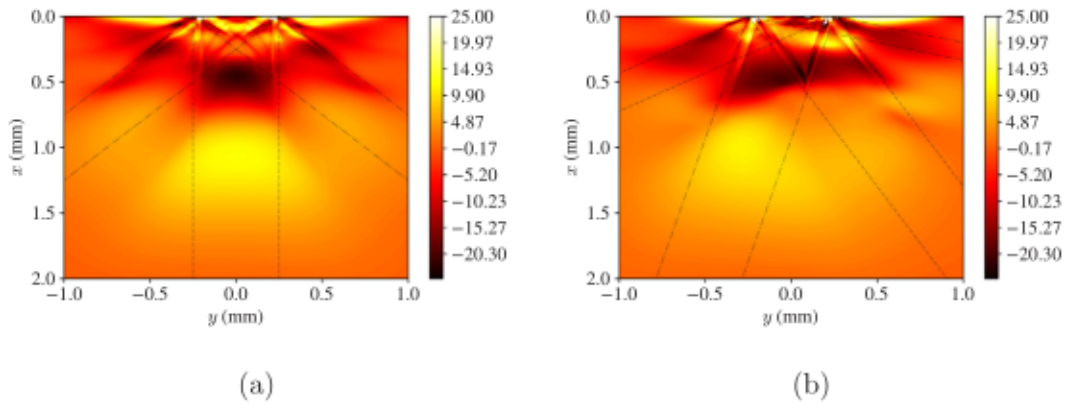
Fig. 6. Residual stresses σ_{22} (MPa) for a single impact on a single crystal (enlarged visual). Black dashed lines correspond to the slip directions of slip system 1, and black dashed/dotted lines correspond to the slip directions of slip system 2. (a) Crystal orientation defined by $\varphi_1 = 0$. (b) Crystal orientation defined by $\varphi_1 = \pi/6$.
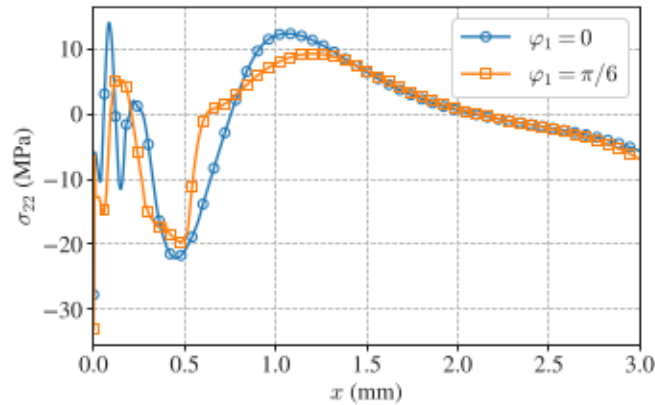

Fig. 7. Spatial profiles of residual stresses in a single crystal as a function of depth, for a line corresponding to the laser impact axis ($y = 0$), for crystal orientations $\varphi_1 = 0$ and $\varphi_1 = \pi/6$.

and $\varphi_1 = \pi/6$ show the same trends, with a pronounced influence of orientation near the surface ($x \leq 0.5$ mm). Although of the same order of magnitude, the stresses for $\varphi_1 = 0$ show a slightly higher tensile peak than the profile for $\varphi_1 = \pi/6$. The depth affected by the residual compressive stresses, which is a quantity that can characterize the efficiency of the laser shock treatment, is however lower with the $\varphi_1 = \pi/6$ orientation.

4.2. Numerical simulation of elastic–plastic laser shock wave in polycrystalline aggregates

We continue with the simulation of elastic–plastic shockwave propagation in the case of a polycrystal. The objective here is to illustrate the influence of a fine microstructure on the residual fields caused by the passage of the stress wave.

Simulations parameters. To begin with, two simulations are performed on two different microstructures, which vary only in the number, position and shape of the grains. All other parameters are strictly identical to those of Section 4.1. The average number of grains will be taken equal to $\eta = 6000$. Such a value allows us to obtain an average grain size of 40 µm. We thus have on average 12 grains inside the laser spot. In the microstructures, the grains are distributed using an uniform distribution in the plane of the simulation. Then, 50 orientations are taken equally spaced between $\varphi_1 = -\pi/2$ and $\varphi_1 = \pi/2$. For such a 2D problem, this is enough to reach an effective behavior of the polycrystal that is very close to isotropic. Our results are valid for such randomly oriented polycrystalline aggregates. We did not investigate the effect of crystallographic textures and the possible coupling with grain size. To increase the meshing of the grains, the number of nodes is now chosen as $N_x = N_y = 1000$. These two microstructures are represented on Fig. 8.

Plastic strains field. We first present in Fig. 9 the accumulated plastic strain γ in the case of the two microstructures of Fig. 8.

The results in Fig. 9 show that the accumulated plastic strain distribution seems to reflect the geometrical distribution of the grains. This result was expected, since the orientation of the grains directly influences the symmetric Schmid tensors of the slip
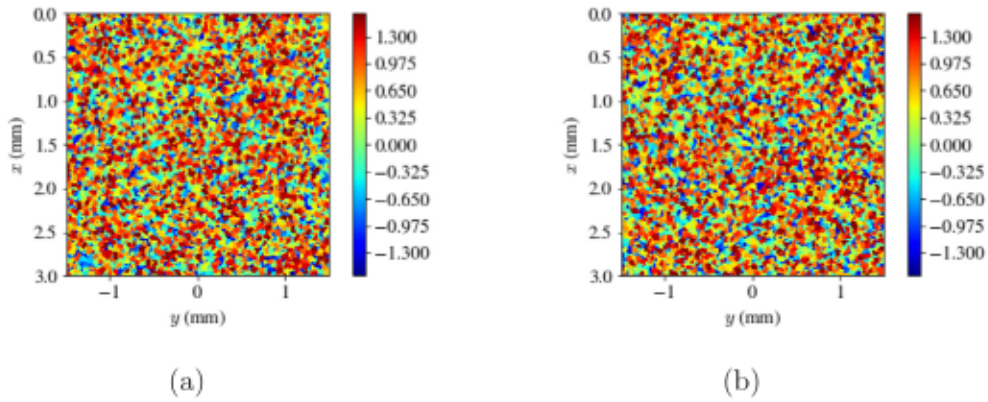
Fig. 8. Two random microstructures. The color scale indicate the Euler angle φ_1 (rad) used for the simulations. (a) Microstructure 1. (b) Microstructure 2.
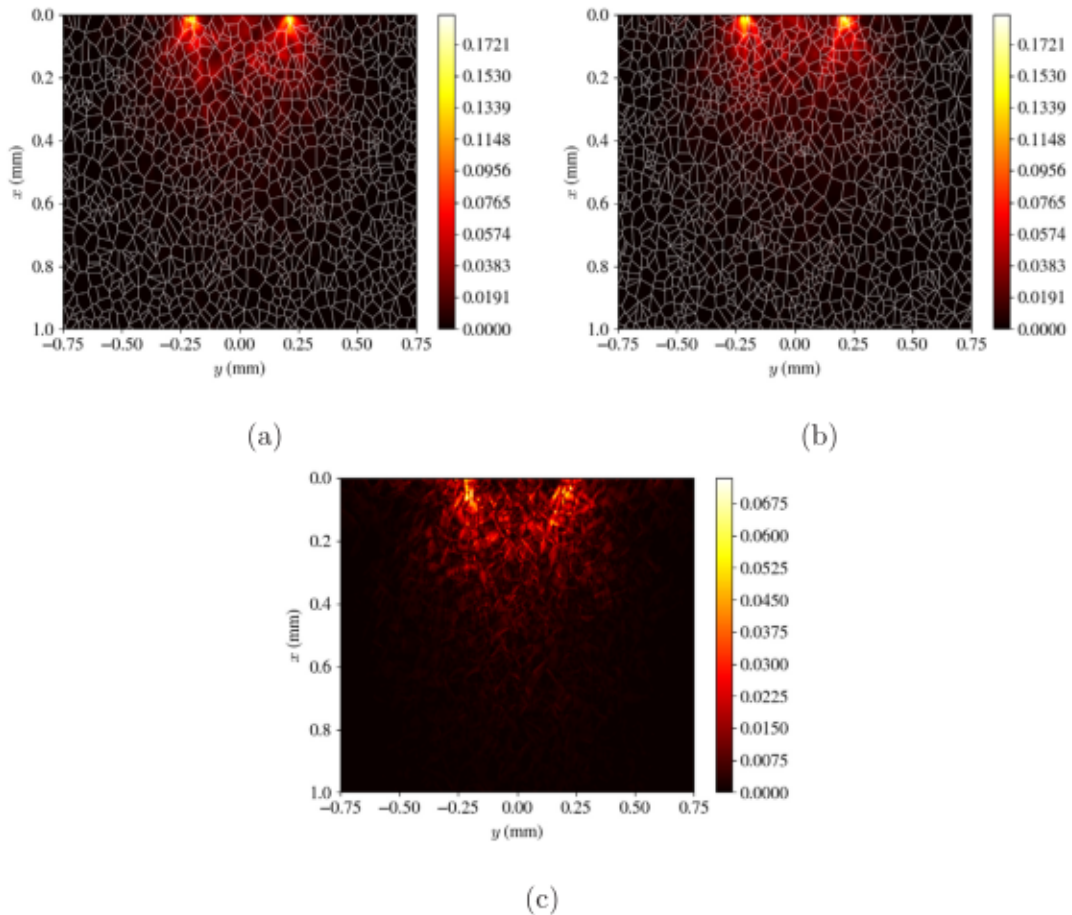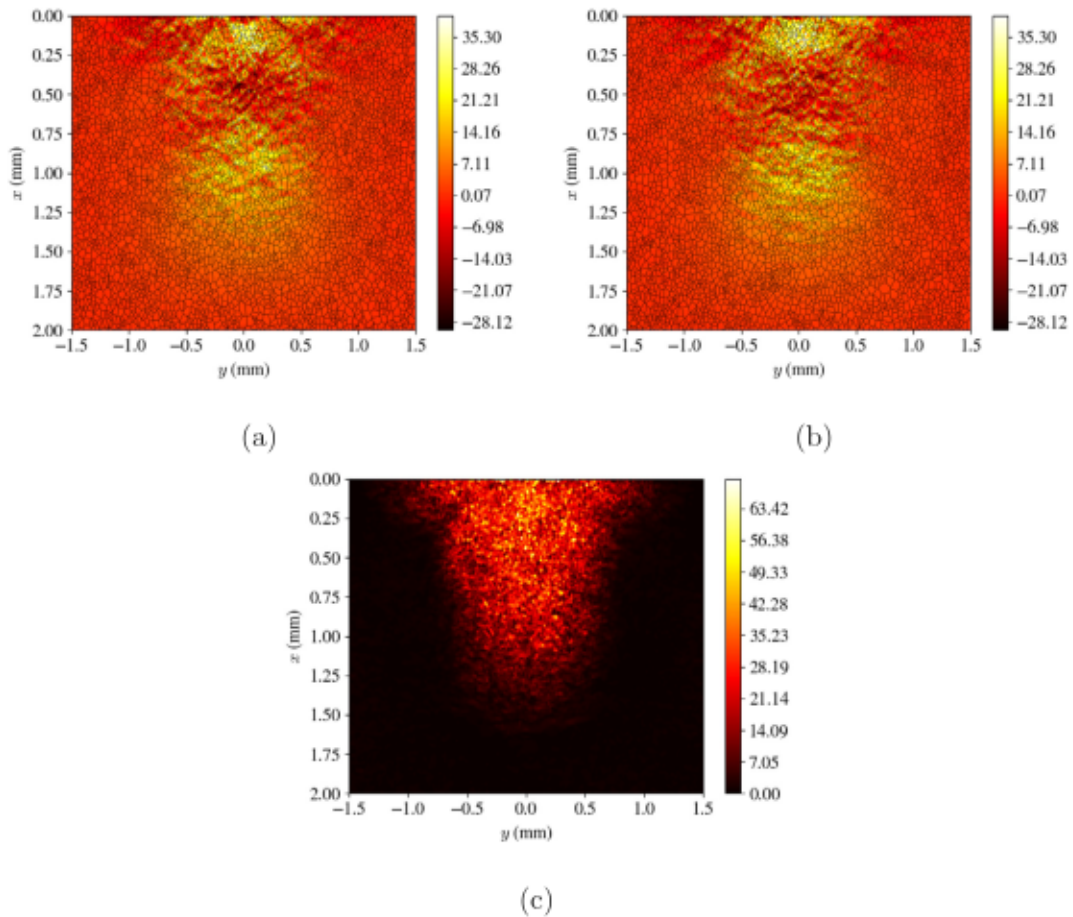

Fig. 9. Accumulated plastic strain distribution γ. The white lines represent the grain boundaries. (a) Microstructure 1. (b) Microstructure 2. (c) Absolute error between the two accumulated plastic strain distributions.

systems, leading to these discontinuous plastic strain values from one grain to another. High values of global accumulated plastic strain are always present at the edges of the laser impact. Furthermore, the plastic strain distributions also appear to show multiple localization bands, propagating radially from the laser impact edges. Moreover, some concentration of plastic strain seems to take place at the grain boundaries. It is difficult to interpret this observation, as it depends on many factors: grain orientation, local stress state, behavior of neighboring grains, etc. The microstructures used as input to the simulations are different, so the fields in Fig. 9 are locally different, but the two simulations are similar from a global point of view. This observation seems to suggest that for a

Fig. 10. Residual stress distribution σ_{22} (MPa). The black lines represent the grain boundaries. (a) Microstructure 1. (b) Microstructure 2. (c) Absolute error between the two residual stresses distributions.

grain size fine enough compared to the laser spot size, the accumulated plastic strain field changes little from one microstructure to another in general. Fig. 9(c) shows the absolute error between the two accumulated plastic strain distributions, emphasizing the discrepancies caused by the microstructures. This error distribution displays grain-like shapes, though they do not correspond entirely to either of the microstructures of Fig. 8.

Residual stress field. In continuation of the analysis, we now show in Fig. 10 the residual stresses induced in the microstructures.

Similar conclusions to those in Fig. 9 can be drawn for Fig. 10. The residual stress distribution directly reflects the grain distribution of the microstructure, and thus varies from one microstructure to another. This is also emphasized by Fig. 10(c), where the absolute errors between the two residual stresses distributions is presented, displaying non zero values all over the affected zone. An alternative representation is to compute the average stress *in each grain*. This view is closer to the results that would be obtained by an X-ray diffraction analysis, where average fields per diffracting grain are measured. These results are illustrated in Fig. 11 with the stress distribution along lines on the surface of the specimen, and in depth at the center of the impact.

Fig. 11 shows that, for the microstructures considered, the surface and depth results are relatively close, and seem to show the same average behavior, while differing in their fluctuations. The residual stresses are tensile at the edge of the patch (Fig. 11(a)), as a consequence of stress balancing across the domain. This presence of tensile stresses is independent of the d/L_y ratio, and can be observed also for macroscopic models (see for example Morin et al., 2021). If the stresses presented are in compression at the center of the surface patch, they are only in compression for a very small thickness (~0.1 mm), before briefly switching to tension at $x \sim 0.2$ mm (Fig. 11(b)). The residual stress profile at depth nevertheless shows a distinctly compressive zone along the center of the impact (0.25 mm $\leq x \leq$ 0.75 mm).

The conclusion of this section is therefore that the consideration of a microstructure influences the residual mechanical fields, insofar as a given microstructure directly influences the distribution of residual stresses obtained. However, the role of the ratio between the average grain size and the laser spot size has yet to be established. This aspect will be discussed in the next section.
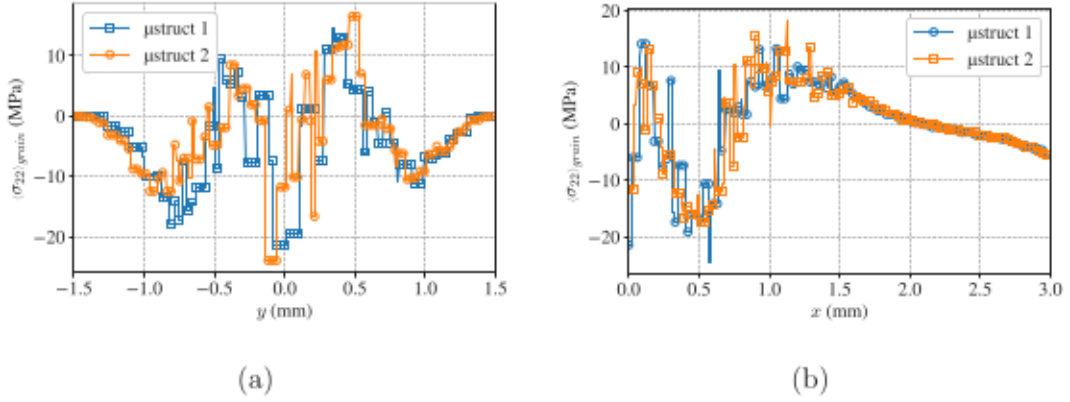
Fig. 11. Distribution of residual stresses σ_{22} (MPa) averaged by grains. (a) At the surface ($x = 0$). (b) At depth ($y = 0$).
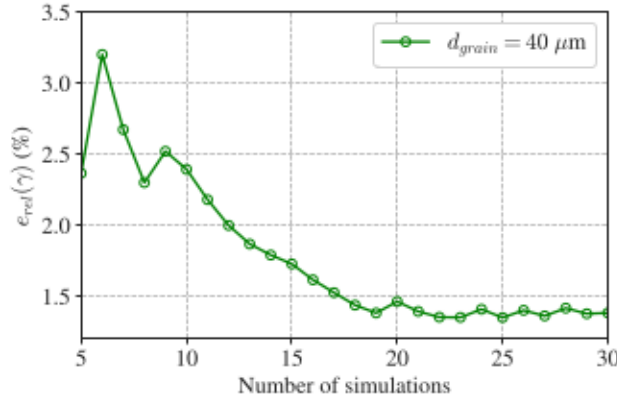

Fig. 12. Evolution of the relative error on the accumulated plastic strain at the center of the impact obtained with i simulations.

4.3. A statistical study of the residual mechanical fields

4.3.1. Description of the statistical approach

As illustrated by Figs. 9 and 10, the random nature of the microstructures generated and used in the simulations greatly influence the results. In order to quantify the influence of the microstructure on the different mechanical fields, we make use of a statistical approach of the results to obtain statistical information on the mechanical fields. To do this, simulations similar to those whose results are presented in Figs. 9 and 10 have been performed for a large number of different microstructures. These simulations are performed with the same parameters, with only different Voronoi tesselations from one simulation to another. The results are no longer considered one by one, but used to determine average mechanical fields and their statistical properties. In this way, we will be able to quantify an average behavior of the polycrystal through simulation, while identifying "extreme" behaviors or responses.

We need for this approach a measure allowing to determine if the number of simulations we realized is sufficient. For that, we are inspired by the approach of Kanit et al. (2003), which seek in their work to determine the size of the Representative Elementary Volume to be chosen in order to correctly estimate effective properties. An absolute error is then defined as:

$$e_{rel} = \frac{2D_Z}{\overline{Z}\sqrt{N}}, \tag{42}$$

where D_Z is the standard deviation of the realizations of the variable Z, $\overline{Z}$ is the average of the realizations of Z, and N is the total number of realizations. Here, the analysis has been made considering the statistical moments of the average of the accumulated plastic strain γ in a zone at the center of the impact ($-0.1 \leq y \leq 0.1$ and $x = 0$, see Fig. 14(a)), for a number of realizations. Depending on the number of simulations performed, we obtain the curve presented in Fig. 12.

The relative error reaches a plateau (1.4%) after 19 realizations. In the following, we will present statistical average based on 30 realizations, which is sufficient to obtain a complete statistical description of the accumulated plastic strain field with a relative accuracy lower than 1.5%.
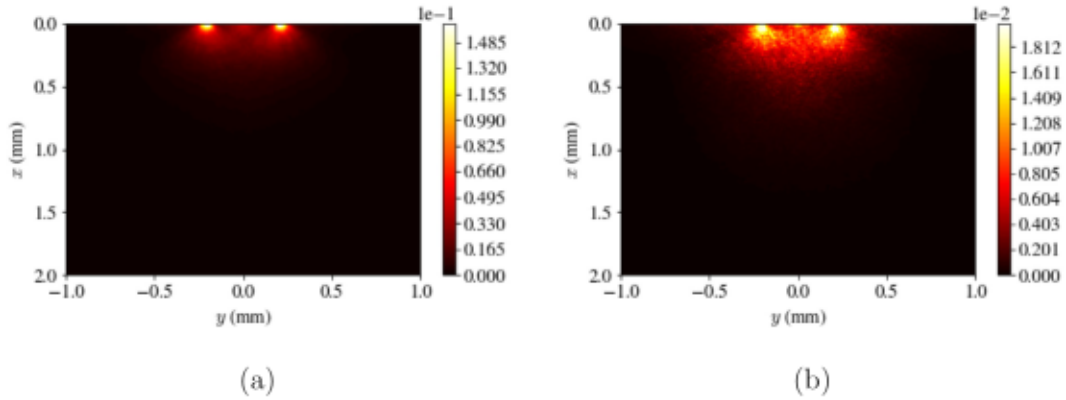
Fig. 13. Statistical properties of the accumulated plastic strain field obtained over 30 simulations. (a) Mean field. (b) Standard deviation field.
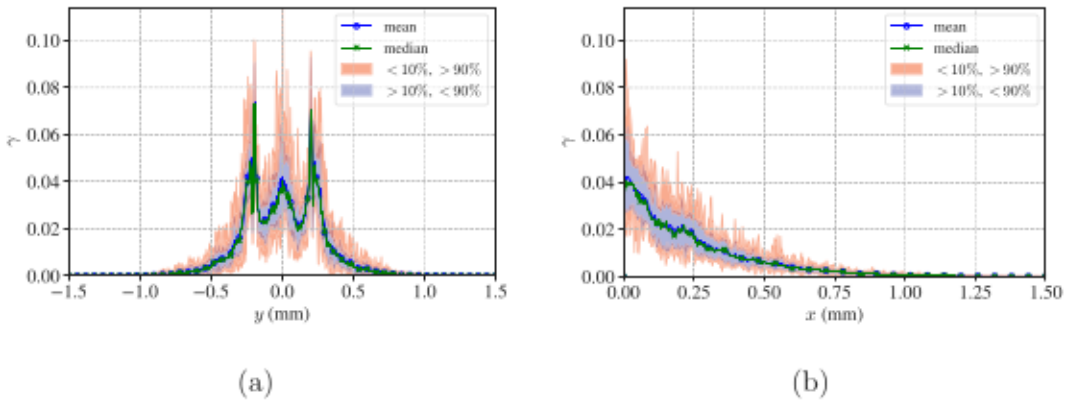

Fig. 14. Mean field of global accumulated plastic strain. (a) Values of the field at the specimen surface ($x = 0$). (b) Values of the field at depth, at the center of the impact ($y = 0$).

4.3.2. Plastic strain field

We start by illustrating the approach by presenting maps of the average accumulated plastic strain, and of the standard deviation on this strain in Fig. 13, computed over 30 simulations. The mean field has a smooth distribution (i.e. no visible influence of microstructures), and is symmetrical with respect to $y = 0$. The standard deviation exhibits more variations, and is particularly pronounced at the edges of the laser spot. Note that the standard deviation on γ is one order of magnitude below the mean field, indicating large field fluctuations.

We also present results of the statistical approach related to the accumulated plastic strain γ (Fig. 14) and the rotation of the crystal lattice ω (Fig. 15) along particular lines: on the surface ($x = 0$) and in depth at the center of the impact ($y = 0$). The different simulations carried out to obtain these results allow us to obtain not only the mean fields, but also the median fields, and to determine intervals containing the values between the percentile at 10% and 90%, in order to obtain more information on the distribution of the results.

The accumulated plastic strain at the surface (Fig. 14(a)) shows a symmetrical profile with respect to the center of the impact, with values mostly centered around the mean and median, especially within the impact. Values are more dispersed in depth (Fig. 14(b)). On the surface and in the center of the impact ($x = 0, y = L_y/2$), the largest fluctuations are of the order of 300% between the lowest and largest values obtained with the different microstructures. As seen previously, the rotation of the crystal lattice is also a marker of plasticity, and is presented in Fig. 15. In contrast to the overall average accumulated plastic strain, the average crystal lattice rotation is antisymmetric at the surface with respect to the impact center, with values highly centered around the mean and median. Values at depth along a line at the center of the impact are not shown, but are nearly zero. The rotations of the crystal lattice are thus induced preferentially at the edges of the laser spot, where the stress state is mainly in shear.

4.3.3. Residual stress field

We now present the results for the residual stresses given in Fig. 16 along the surface and in depth.

Fig. 16(a) shows that the mean and median values at the center of the impact are in compression, but the values attainable in some configuration by the stresses can also be in tension (a standard deviation of ∼20 MPa at $x = 0$ and $y = L_y/2$, for a mean
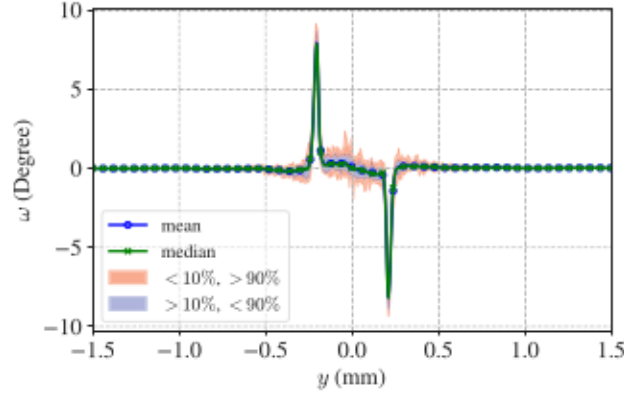
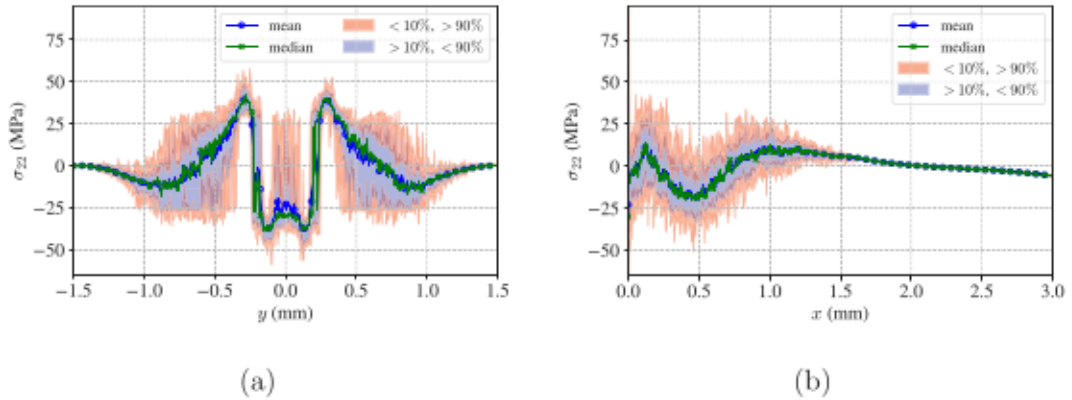**Fig. 15.** Average field of rotation of the crystal lattice on the surface ($x = 0$).

Fig. 16. Mean field of residual stresses. (a) Surface values ($x = 0$). (b) In-depth values at the center of the impact ($y = 0$).

value of ~ -20 MPa). The depth profile in Fig. 16(b) shows that the distribution of residual stresses can be close to zero over the entire thickness affected by the average residual stresses in compression. Theoretically, such residual stress values can decrease the effectiveness of the laser shot peening treatment, if these values are not too localized within the impact. If this situation occurs in a specimen or structure, these would be locations where a crack or defect could preferentially initiate, despite the fact that residual stresses are on average compressive in the rest of the affected area.

4.4. Effect of the microstructure on the backface velocity

In addition to the residual fields, we study the effect of the microstructure on the backface velocity. Indeed, the velocity of the rear face (opposite of the laser impact) of the specimen can be measured by VISAR technique, for thin (few hundreds of microns) specimens (Seddik et al., 2022; Ayad et al., 2022a,b). This backface velocity can be used to identify the material's constitutive relation at the huge strain-rate encountered during LSP. For all the results that have been shown so far, the average grain size has been kept constant. However, it is a parameter that can primarily influence the heterogeneity of the mechanical field. In the following, we will consider three different average grain sizes: 40 μm, 80 μm and 160 μm.

Simulations parameters. It is necessary here to slightly modify the parameters of the simulations. Indeed, the study of the velocity at the back face requires a thin sample, so that the stress wave is not too attenuated when it arrives at the back face, in order for the results to contain information on the elasto-visco-plastic behavior. We therefore change the dimensions of the model, and use $L_x = 0.5$ mm and $L_y = 3$ mm. Only the thickness of the sample has been reduced. All other parameters remain the same as in the previous simulations. The boundary condition of the face $x = L_x$ is this time modeled as a free surface, to ensure the full reflection of the stress wave.

Typical microstructures used for the backface velocity simulations are shown in Fig. 17.

Simulations results. Again, 30 simulations are performed for each of the microstructure sizes presented in Fig. 17. The backface velocity profiles are extracted at the point ($x = L_x, y = 0$).

In Fig. 18, we present the statistical distribution of the backface velocity profiles. As with the results in Section 4.3, Fig. 18 presents the mean, median, and a band containing the values taken by the backface velocity for all simulations. It is immediately
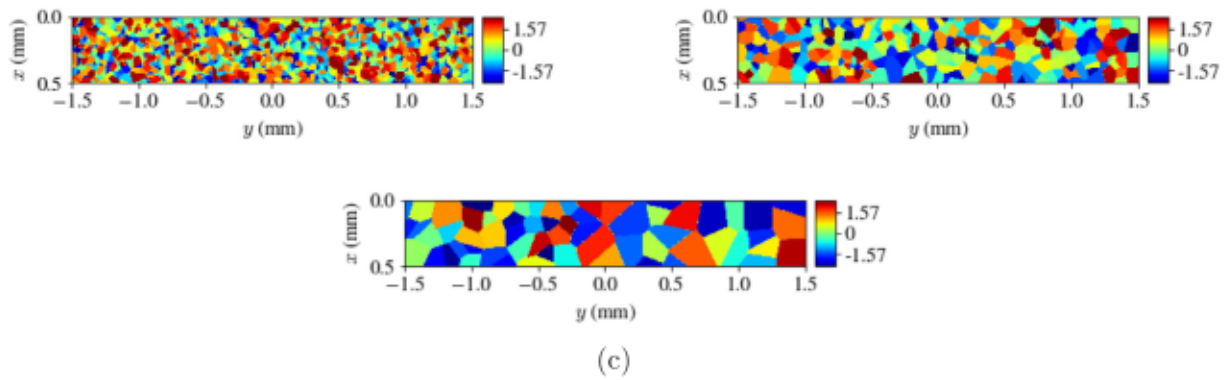
Fig. 17. Typical microstructures used for backface velocity calculations. (a) Average grain size of 40 μm. (b) Average grain size of 80 μm. (c) Average grain size of 160 μm.
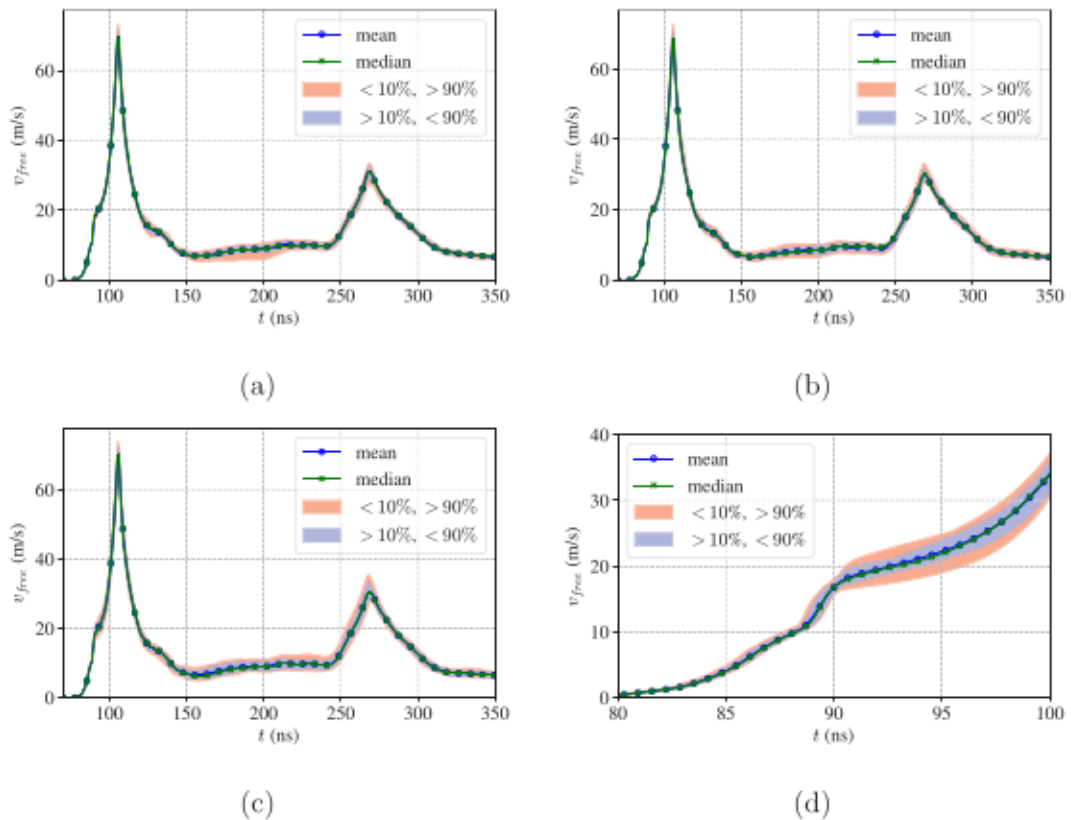
Fig. 18. Average backface velocity profiles. (a) For average grain size of 40 μm. (b) For average grain size of 80 μm. (c) For average grain size of 160 μm. (d) Zoom to precursor for average grain size of 160 μm.

noticeable that the backface velocity values seem very centered around an average behavior. A thickening of the band of values can nevertheless be noticed. The larger the average grain size, the more the results are scattered between two statistically equivalent microstructures. The first peak of the velocities is little affected by the size of the microstructure except at the level of the elastic precursor (~19 MPa, 80 ns), where the dispersion of the values increases with the average grain size of the microstructure. The

minimum velocity introducing plastic strain can thus vary from one microstructure to another, in particular for a microstructure with large grains (see Fig. 18(c)). Moreover, the inflection of the velocity profile at the back face (average or median) at the level of the elastic precursors is smooth for the plots of Fig. 18, and thus reflects a continuous transition from elasticity to plasticity.

5. Discussion

The introduction of material heterogeneity in the description of the polycrystalline material has thus a direct influence on the mechanical fields, both residual and related to the propagation. This is consistent with other works from the literature, notably Sunny et al. (2021) who presented equivalent plastic strain fields induced by a laser impact in a polycrystal microstructure which display the shape of the grains, as in Fig. 9. However the authors considered in their work a Johnson-Cook type behavior for the grains, while we adopt a crystal plasticity model. Separately, Vukelić et al. (2009) presented simulations of a laser impact on a bicrystal using a crystal plasticity law. Their results also show discontinuities at the grain boundary in the plastic strain fields, as well as in the lattice rotation fields. Nonetheless the computed residual stresses are continuous and the grain boundary is almost invisible when looking at the stress field. It is worth noting that the authors use the complete set of slip systems for aluminum contrary to this work, and a much smaller spot diameter of 12 μm, which greatly influences the residual stress field.

Unlike the residual stress field which is difficult to experimentally analyze at this scale, it is possible to experimentally measure the lattice rotation field, which is a marker of the plasticity in the polycrystal. In this context, Chen et al. (2004) measured the lattice rotation after a laser shock on an aluminum single crystal using X-ray microdiffraction techniques (see for example Fig. 9(a) of their work). These lattice rotation profiles are similar in trend to our Fig. 15: the edges of the laser spot are particularly marked, with rotations of the order of $\pm 3°$ ($\pm 8°$ in our case), and zero rotation at the center of the impact. The discrepancies can be explained notably by the difference of spot diameters and of pressure spatial distribution profiles. These similarities between the simulated results and experimental profiles could be exploited for model validation.

However, it is important to note that a quantitative comparison with experimental data will require a more complete modeling. A 2D plane strain modeling was used not to increase dramatically the computation cost (here ~10 h for the propagation and stress redistribution). A direct improvement would be to consider a 3D model, so as not to make any simplifying hypotheses, either about the geometry of the problem or the mechanical description (a complete set a of slip systems could then be used). This would also allow the use of microstructures more representative of polycrystalline material, in terms of grain morphology and orientations distribution. However a great computational cost can be expected for a 3D model, which could prove prohibitive for small grain sizes, which require a fine mesh. For LSP, 3D model are currently used to study the overlapping parameters (Larson et al., 2019; Bhamare et al., 2013), with however the work of Chen et al. (2007), using a 3D finite element model to study the effect of micro-LSP on Aluminum single crystals.

A possibility to push the study further while avoiding too large model would be to consider homogenized models, as done in Lapostolle et al. (2022a) in the case of a laminate elastic–plastic material. We have shown through a large number of simulations that it is possible to compute an average behavior of the microstructure. It would be particularly interesting to show that it is possible to determine an equivalent macroscopic model (either homogenized or identified from a macroscopic law) allowing to calculate directly the average behavior of the microstructure and the statistical fluctuations of the mechanical fields, provided that the average size of the grains of the microstructure is small enough. This approach would have the advantage of being much more efficient in computation time, since the mesh would not need to be as fine as for a full field model.

Fig. 16(a) in particular showed that despite a mean behavior in compression at the surface and in the center of the impact, it is possible to have a realization of a microstructure that leads to less compressive residual stresses, or even traction stresses. During a cyclic loading, a crack would be likely to initiate at these loci. The fatigue behavior is thus driven by the worst case scenario, which simulations as the ones proposed in this work can help predict. The residual stresses also present strong gradients at the surface. Residual stresses are impacted by the gradients of plastic strains, which are also strong in the immediate vicinity of the impacted surface. Though such fields are not shown in this work, the mean accumulated plastic strain field of Fig. 13(a) shows a rapid decrease from the surface when the depth increases. The high standard variation in Fig. 13(b) close to the surface also indicates fluctuations of the plastic strain fields, and thus of the residual stress field. One must however keep in mind that we consider the case of a single impact, while overlap is often used in industrial configuration. Laser spot overlapping is believed to homogenize the stress state at the specimen surface (Xiang et al., 2021; Hfaiedh et al., 2015). Moreover, the stress values at the center of the impact in Fig. 16(a) are mostly centered around the mean values. All this is dependent on the material used, and may not be the same for different material parameters. The link between the microstructure characteristics and the dispersion of the mechanical fields, especially for the residual stresses, would be an important addition to this study. This would allow, for a given microstructure, to help quantify the difference that can be expected between two measurements of residual stresses analysis performed between two samples treated by laser shock peening in an equivalent manner. Moreover, such information would allow to quantify the level of residual stresses that can really be expected in a structure or a sample, from a macroscopic simulation giving access to an average behavior, and thus to optimize the design steps, taking into account the most conservative case.

A more complete study of the influence of the grain size is another perspective of this work. Particularly, the link between the average size or shape of the grains and the dispersion of the mechanical fields could be assessed. Given the results, it could help interpret experimental results. For instance, the discrepancies between two similar backface velocity measurement, as in Ayad et al. (2022a), could be the result of the locally different microstructures. More specifically regarding the velocity profiles of Fig. 18, the low dispersion can be linked to the low contrast of the mechanical properties in the direction of the propagation (the velocities between to grain can only increase here up to 2.5%). Applying Eq. (42) to the maximum velocity would yield diminishing errors

when one increases the number of simulations. For large numbers of simulations (more than 25), the errors for the different average grains sizes are close (~1.4%), but increase with the average size of the grains. This seems to indicate that a microstructure with large grains has a larger dispersion of the velocity or stress fields. Results following this trend can be found in the work of Segurado and Lebensohn (2021) (see Fig. 9 of their work), who indicate that a low anisotropy of the grains (i.e. a low Zener coefficient) results in a lowest drop in wave group velocity than for a higher anisotropy. Additionally, the bigger the grain size, the bigger the velocity drop. This dispersion that the microstructure induces on the wave front is also reported in Case and Horie (2007), who studied the dispersion along a plane wave front propagating in polycrystalline copper. Moreover, knowing the dispersion of the residual stresses induced by a given microstructure could help accounting for the worst case scenario when trying to introduce compressive residual stresses. In the case of the residual fields, the average grain size influences both the probability of finding similar grain orientations in a given volume, and the density of grain interfaces, both factors being expected to play a role in the dispersion of the fields. Their influence should thus be studied in future works.

6. Conclusion

This article was focused on the influence of a polycrystalline microstructure on the propagation of a stress wave and the induced plastic strain and residual stress fields. For this, a 2D plane strain formalism was considered. Two slip systems were used at the crystal scale. The propagation of the elastic stress wave has been modeled by a hyperbolic PDE system, solved with an explicit Godunov numerical scheme. To this resolution is added a visco-plastic crystal plasticity model. First simulations on single crystals allow to observe localization bands of the plastic strain, oriented according to the directions of the slip systems. In this case, the residual stresses are dependent on the chosen crystal orientation, making them more or less compressive. The incorporation of a Voronoi tessellation type microstructure greatly influences the distribution of plastic strains and residual stresses, which bear the mark of the microstructure. In the case of residual stresses, high concentrations are observed at the grain boundaries, which do not depend on the mesh size or on the heterogeneity of the mechanical properties. The average influence of the microstructure is then studied, by performing a statistical approach of the problem. Through a large number of simulations, we found that the mechanical fields (residual or relative to the propagation of the stress wave) tend to the same average regardless of the average grain size given for the microstructures. This feature is consistent with the macroscopic models classically used for laser shock (such as the Johnson-Cook model), which do not show any dependence on grain size. However, we have shown that the microstructure induces a dispersion of the mechanical fields. This dispersion is important, because it can give information on the worst case for fatigue resistance for example. In particular, the residual stresses induced by the laser shock simulated in the microstructures can be more or less in compression at the center of the impact. The work presented in this article opens the following perspectives:

- This work could be extended to a 3D model, in order to include a complete and realistic set of slip systems, as well as a description of the microstructure more representative of a polycrystalline material.
- The role of the grain size on the residual mechanical field is still to be thoroughly investigated, in particular its influence on the dispersion of the residual fields. A small grain size means that there is a higher probability of having similar orientations in a given volume, and thus a lower dispersion of the mechanical fields, but also a higher density of grain boundaries, which may increase the dispersion. The contribution of these phenomenon is to be assessed.
- The computational cost of the simulation could be reduced by considering a homogenized material, that either corresponds to the behavior obtained by averaging several simulation over different microstructures, or by applying a homogenization scheme to the elasto-visco-plastic polycrystalline aggregate.
- Laser loading with overlapping could also be added to the simulations, to see the effect not only of several shots with this polycrystal work frame, but also on the dispersion of the mechanical fields.

Declaration of competing interest

The authors declare that they have no known competing financial interests or personal relationships that could have appeared to influence the work reported in this paper.

Data availability

No data was used for the research described in the article.

Acknowledgments

Appendix A. Numerical method for the 2D stress wave propagation

In this appendix we detail the numerical resolution of the 2D stress wave equation in Eq. (23). The Godunov numerical scheme is used according to Leveque (2002), which gives expressions for the fluxes F and G of Eq. (27):

$$
\begin{cases}
F_{i-1/2,j}^n = A^+ U_{i-1,j}^n + A^- U_{i,j}^n - \dfrac{\Delta t}{2\Delta y}\left(A^- B^- \left(U_{i,j+1}^n - U_{i,j}^n \right) + A^+ B^- \left(U_{i-1,j+1}^n - U_{i-1,j}^n \right) + \right. \\
\qquad\qquad \left. A^- B^+ \left(U_{i,j}^n - U_{i,j-1}^n \right) + A^+ B^+ \left(U_{i-1,j}^n - U_{i-1,j-1}^n \right) \right) \\[4pt]
F_{i+1/2,j}^n = A^+ U_{i,j}^n + A^- U_{i+1,j}^n - \dfrac{\Delta t}{2\Delta y}\left(A^- B^- \left(U_{i+1,j+1}^n - U_{i+1,j}^n \right) + A^+ B^- \left(U_{i,j+1}^n - U_{i,j}^n \right) + \right. \\
\qquad\qquad \left. A^- B^+ \left(U_{i+1,j}^n - U_{i+1,j-1}^n \right) + A^+ B^+ \left(U_{i,j}^n - U_{i,j-1}^n \right) \right) \\[4pt]
G_{i,j-1/2}^n = B^+ U_{i,j-1}^n + B^- U_{i,j}^n - \dfrac{\Delta t}{2\Delta x}\left(B^- A^- \left(U_{i+1,j}^n - U_{i,j}^n \right) + B^+ A^- \left(U_{i+1,j-1}^n - U_{i,j-1}^n \right) + \right. \\
\qquad\qquad \left. B^- A^+ \left(U_{i,j}^n - U_{i-1,j}^n \right) + B^+ A^+ \left(U_{i,j-1}^n - U_{i-1,j-1}^n \right) \right) \\[4pt]
G_{i,j+1/2}^n = B^+ U_{i,j}^n + B^- U_{i,j+1}^n - \dfrac{\Delta t}{2\Delta x}\left(B^- A^- \left(U_{i+1,j+1}^n - U_{i,j+1}^n \right) + B^+ A^- \left(U_{i+1,j}^n - U_{i,j}^n \right) + \right. \\
\qquad\qquad \left. B^- A^+ \left(U_{i,j+1}^n - U_{i-1,j+1}^n \right) + B^+ A^+ \left(U_{i,j}^n - U_{i-1,j}^n \right) \right).
\end{cases}
\tag{A.1}
$$

The matrices A^+, A^-, B^+ and B^- are defined by (only for the matrix A for the sake of conciseness):

$$
A^+ = PD^+P^{-1} \quad\text{and}\quad A^- = PD^-P^{-1},
\tag{A.2}
$$

with

$$
D_{ij}^+ = \delta_{ij}\max\left(0, \lambda_j\right) \quad\text{and}\quad D_{ij}^- = \delta_{ij}\min\left(0, \lambda_j\right),
\tag{A.3}
$$

where λ_j denotes the jth eigenvalue of the matrix A, δ_{ij} is the Kronecker symbol, and P is the transition matrix of A.

In this way, the term $U_{i,j}^{n+1}$ is calculated by linear combination of the values of U^n. It is thus possible to calculate the state at the next time increment of the whole system with

$$
X^{n+1} = QX^n,
\tag{A.4}
$$

with $X^n = \left(U_{1,1}^n U_{1,2}^n \cdots U_{1,N_y}^n U_{2,1}^n \cdots U_{i,j}^n \cdots U_{N_x,1}^n \cdots U_{N_x,N_y}^n \right)^T$, where N_x and N_y are the numbers of nodes in the spatial domain in the x and y directions respectively. Q is a matrix of size $(5N_x N_y)\times(5N_x N_y)$ constructed using the matrices A^+, A^-, B^+ and B^-. Eq. (A.4) thus allows to compute the state of the system at increment $n+1$.

Appendix B. System for the residual stresses modeling

In this appendix we give details about the resolution of the stress redistribution leading to the computation of the residual stresses. The system of equations to solve is the one given in Eq. (35). The static equilibrium, accounting for the heterogeneity of the material, thus gives the following system:

$$
\begin{cases}
\dfrac{\partial u_x}{\partial x}\left(\dfrac{\partial C_{1111}}{\partial x} + \dfrac{\partial C_{1112}}{\partial y} \right) + \dfrac{\partial u_x}{\partial y}\left(\dfrac{\partial C_{1112}}{\partial x} + \dfrac{\partial C_{1212}}{\partial y} \right) + C_{1111}\dfrac{\partial^2 u_x}{\partial x^2} + C_{1212}\dfrac{\partial^2 u_x}{\partial y^2} + 2C_{1112}\dfrac{\partial^2 u_x}{\partial x\partial y} + \\[4pt]
\dfrac{\partial u_y}{\partial x}\left(\dfrac{\partial C_{1112}}{\partial x} + \dfrac{\partial C_{1212}}{\partial y} \right) + \dfrac{\partial u_y}{\partial y}\left(\dfrac{\partial C_{1122}}{\partial x} + \dfrac{\partial C_{2212}}{\partial y} \right) + C_{1112}\dfrac{\partial^2 u_y}{\partial x^2} + C_{2212}\dfrac{\partial^2 u_y}{\partial y^2} + \dfrac{\partial^2 u_y}{\partial x\partial y}\left(C_{1122} + C_{1212} \right) = \\[4pt]
\varepsilon_p\left(\dfrac{\partial C_{1111}}{\partial x} + \dfrac{\partial C_{1112}}{\partial y} - \dfrac{\partial C_{1122}}{\partial x} - \dfrac{\partial C_{2212}}{\partial y} \right) + 2\varepsilon_{p,12}\left(\dfrac{\partial C_{1112}}{\partial x} + \dfrac{\partial C_{1212}}{\partial y} \right) + \dfrac{\partial \varepsilon_p}{\partial x}\left(C_{1111} - C_{1122} \right) + \\[4pt]
\dfrac{\partial \varepsilon_p}{\partial y}\left(C_{1112} - C_{2212} \right) + 2C_{1112}\dfrac{\partial \varepsilon_{p,12}}{\partial x} + 2C_{1212}\dfrac{\partial \varepsilon_{p,12}}{\partial y}; \\[4pt]
\dfrac{\partial u_x}{\partial x}\left(\dfrac{\partial C_{1112}}{\partial x} + \dfrac{\partial C_{1122}}{\partial y} \right) + \dfrac{\partial u_x}{\partial y}\left(\dfrac{\partial C_{1212}}{\partial x} + \dfrac{\partial C_{2212}}{\partial y} \right) + C_{1112}\dfrac{\partial^2 u_x}{\partial x^2} + C_{2212}\dfrac{\partial^2 u_x}{\partial y^2} + \dfrac{\partial^2 u_x}{\partial x\partial y}\left(C_{1122} + C_{1212} \right) + \\[4pt]
\dfrac{\partial u_y}{\partial x}\left(\dfrac{\partial C_{1212}}{\partial x} + \dfrac{\partial C_{2212}}{\partial y} \right) + \dfrac{\partial u_y}{\partial y}\left(\dfrac{\partial C_{2212}}{\partial x} + \dfrac{\partial C_{2222}}{\partial y} \right) + C_{1212}\dfrac{\partial^2 u_y}{\partial x^2} + C_{2222}\dfrac{\partial^2 u_y}{\partial y^2} + 2C_{2212}\dfrac{\partial^2 u_y}{\partial x\partial y} = \\[4pt]
\varepsilon_p\left(\dfrac{\partial C_{1112}}{\partial x} + \dfrac{\partial C_{1122}}{\partial y} - \dfrac{\partial C_{2212}}{\partial x} - \dfrac{\partial C_{2222}}{\partial y} \right) + 2\varepsilon_{p,12}\left(\dfrac{\partial C_{1212}}{\partial x} + \dfrac{\partial C_{2212}}{\partial y} \right) + \dfrac{\partial \varepsilon_p}{\partial x}\left(C_{1112} - C_{2212} \right) + \\[4pt]
\dfrac{\partial \varepsilon_p}{\partial y}\left(C_{1122} - C_{2222} \right) + 2C_{1212}\dfrac{\partial \varepsilon_{p,12}}{\partial x} + 2C_{2212}\dfrac{\partial \varepsilon_{p,12}}{\partial y}
\end{cases}
\tag{B.1}
$$

We recall the following relations:

$$
\begin{cases}
\sigma_{11} = C_{1111}\left(\dfrac{\partial u_x}{\partial x} - \varepsilon_p\right) + C_{1122}\left(\dfrac{\partial u_y}{\partial y} + \varepsilon_p\right) + C_{1112}\left(\dfrac{\partial u_x}{\partial y} + \dfrac{\partial u_y}{\partial x} - 2\varepsilon_{p,12}\right) \\[2mm]
\sigma_{22} = C_{1122}\left(\dfrac{\partial u_x}{\partial x} - \varepsilon_p\right) + C_{2222}\left(\dfrac{\partial u_y}{\partial y} + \varepsilon_p\right) + C_{2212}\left(\dfrac{\partial u_x}{\partial y} + \dfrac{\partial u_y}{\partial x} - 2\varepsilon_{p,12}\right) \\[2mm]
\sigma_{12} = C_{1112}\left(\dfrac{\partial u_x}{\partial x} - \varepsilon_p\right) + C_{2212}\left(\dfrac{\partial u_y}{\partial y} + \varepsilon_p\right) + C_{1212}\left(\dfrac{\partial u_x}{\partial y} + \dfrac{\partial u_y}{\partial x} - 2\varepsilon_{p,12}\right).
\end{cases}
\tag{B.2}
$$

As indicated in Section 3.3, the system is put under the matrix form $MX = f$ (see Eq. (38)). The vector f corresponds to the right-hand side of Eq. (B.2) evaluated numerically. The expression of the matrix M can be further detailed, for indices i and j such that the point (x_i, y_j) is in Ω:

$$
\begin{aligned}
\begin{pmatrix} (M_{11}U_x)_{(j-1)N_x+i} \\ (M_{21}U_x)_{(j-1)N_x+i} \end{pmatrix} &= \begin{pmatrix} h_{11} & h_{12} & h_{13} & h_{14} & h_{15} & h_{16} & h_{17} & h_{18} & h_{19} \\ h_{31} & h_{32} & h_{33} & h_{34} & h_{35} & h_{36} & h_{37} & h_{38} & h_{39} \end{pmatrix} \begin{pmatrix} U_{x,(j-1)N_x+1} \\ U_{x,(j-1)N_x+1} \end{pmatrix} \\[2mm]
\begin{pmatrix} (M_{12}U_y)_{(j-1)N_x+i} \\ (M_{22}U_y)_{(j-1)N_x+i} \end{pmatrix} &= \begin{pmatrix} h_{21} & h_{22} & h_{23} & h_{24} & h_{25} & h_{26} & h_{27} & h_{28} & h_{29} \\ h_{41} & h_{42} & h_{43} & h_{44} & h_{45} & h_{46} & h_{47} & h_{48} & h_{49} \end{pmatrix} \begin{pmatrix} U_{y,(j-1)N_x+1} \\ U_{y,(j-1)N_x+1} \end{pmatrix}.
\end{aligned}
\tag{B.3}
$$

with $U_{x,(j-1)N_x+1} = \left(u_{x,i-1j-1},\ u_{x,ij-1},\ u_{x,i+1j-1},\ u_{x,i-1j},\ u_{x,ij},\ u_{x,i+1j},\ u_{x,i-1j+1},\ u_{x,ij+1},\ u_{x,i+1j+1}\right)^T$, and $U_{y,(j-1)N_x+1}$ being defined in a similar manner. The coefficients h_{ij} are constructed using the finite differences method.

$$
\begin{cases}
h_{11} = \dfrac{C_{1112}}{2\Delta x\Delta y} \\[2mm]
h_{12} = \dfrac{C_{1212}}{\Delta y^2} - \dfrac{1}{2\Delta y}\left(\left(\dfrac{\partial C_{1112}}{\partial x}\right)_{ij} + \left(\dfrac{\partial C_{1212}}{\partial y}\right)_{ij}\right) \\[2mm]
h_{13} = -\dfrac{C_{1112}}{2\Delta x\Delta y} \\[2mm]
h_{14} = \dfrac{C_{1111}}{\Delta x^2} - \dfrac{1}{2\Delta x}\left(\left(\dfrac{\partial C_{1111}}{\partial x}\right)_{ij} + \left(\dfrac{\partial C_{1112}}{\partial y}\right)_{ij}\right) \\[2mm]
h_{15} = -\dfrac{2C_{1111}}{\Delta x^2} - \dfrac{2C_{1212}}{\Delta y^2} \\[2mm]
h_{16} = \dfrac{C_{1111}}{\Delta x^2} + \dfrac{1}{2\Delta x}\left(\left(\dfrac{\partial C_{1111}}{\partial x}\right)_{ij} + \left(\dfrac{\partial C_{1112}}{\partial y}\right)_{ij}\right) \\[2mm]
h_{17} = -\dfrac{C_{1112}}{2\Delta x\Delta y} \\[2mm]
h_{18} = \dfrac{C_{1212}}{\Delta y^2} + \dfrac{1}{2\Delta y}\left(\left(\dfrac{\partial C_{1112}}{\partial x}\right)_{ij} + \left(\dfrac{\partial C_{1212}}{\partial y}\right)_{ij}\right) \\[2mm]
h_{19} = \dfrac{C_{1112}}{2\Delta x\Delta y}
\end{cases}
\qquad
\begin{cases}
h_{21} = \dfrac{C_{1122}}{4\Delta x\Delta y} + \dfrac{C_{1212}}{4\Delta x\Delta y} \\[2mm]
h_{22} = \dfrac{C_{2212}}{\Delta y^2} - \dfrac{1}{2\Delta y}\left(\left(\dfrac{\partial C_{1122}}{\partial x}\right)_{ij} + \left(\dfrac{\partial C_{2212}}{\partial y}\right)_{ij}\right) \\[2mm]
h_{23} = -\dfrac{C_{1122}}{4\Delta x\Delta y} - \dfrac{C_{1212}}{4\Delta x\Delta y} \\[2mm]
h_{24} = \dfrac{C_{1112}}{\Delta x^2} - \dfrac{1}{2\Delta x}\left(\left(\dfrac{\partial C_{1112}}{\partial x}\right)_{ij} + \left(\dfrac{\partial C_{1212}}{\partial y}\right)_{ij}\right) \\[2mm]
h_{25} = -\dfrac{2C_{1112}}{\Delta x^2} - \dfrac{2C_{2212}}{\Delta y^2} \\[2mm]
h_{26} = \dfrac{C_{1112}}{\Delta x^2} + \dfrac{1}{2\Delta x}\left(\left(\dfrac{\partial C_{1112}}{\partial x}\right)_{ij} + \left(\dfrac{\partial C_{1212}}{\partial y}\right)_{ij}\right) \\[2mm]
h_{27} = -\dfrac{C_{1122}}{4\Delta x\Delta y} - \dfrac{C_{1212}}{4\Delta x\Delta y} \\[2mm]
h_{28} = \dfrac{C_{2212}}{\Delta y^2} + \dfrac{1}{2\Delta y}\left(\left(\dfrac{\partial C_{1122}}{\partial x}\right)_{ij} + \left(\dfrac{\partial C_{2212}}{\partial y}\right)_{ij}\right) \\[2mm]
h_{29} = \dfrac{C_{1122}}{4\Delta x\Delta y} + \dfrac{C_{1212}}{4\Delta x\Delta y}
\end{cases}
\tag{B.4}
$$

$$
\begin{cases}
h_{31} = \dfrac{C_{1122}}{4\Delta x\Delta y} + \dfrac{C_{1212}}{4\Delta x\Delta y} \\[2mm]
h_{32} = \dfrac{C_{2212}}{\Delta y^2} - \dfrac{1}{2\Delta y}\left(\left(\dfrac{\partial C_{1212}}{\partial x}\right)_{ij} + \left(\dfrac{\partial C_{2212}}{\partial y}\right)_{ij}\right) \\[2mm]
h_{33} = -\dfrac{C_{1122}}{4\Delta x\Delta y} - \dfrac{C_{1212}}{4\Delta x\Delta y} \\[2mm]
h_{34} = \dfrac{C_{1112}}{\Delta x^2} - \dfrac{1}{2\Delta x}\left(\left(\dfrac{\partial C_{1112}}{\partial x}\right)_{ij} + \left(\dfrac{\partial C_{1122}}{\partial y}\right)_{ij}\right) \\[2mm]
h_{35} = -\dfrac{2C_{1112}}{\Delta x^2} - \dfrac{2C_{2212}}{\Delta y^2} \\[2mm]
h_{36} = \dfrac{C_{1112}}{\Delta x^2} + \dfrac{1}{2\Delta x}\left(\left(\dfrac{\partial C_{1112}}{\partial x}\right)_{ij} + \left(\dfrac{\partial C_{1122}}{\partial y}\right)_{ij}\right) \\[2mm]
h_{37} = -\dfrac{C_{1122}}{4\Delta x\Delta y} - \dfrac{C_{1212}}{4\Delta x\Delta y} \\[2mm]
h_{38} = \dfrac{C_{2212}}{\Delta y^2} + \dfrac{1}{2\Delta y}\left(\left(\dfrac{\partial C_{1212}}{\partial x}\right)_{ij} + \left(\dfrac{\partial C_{2212}}{\partial y}\right)_{ij}\right) \\[2mm]
h_{39} = \dfrac{C_{1122}}{4\Delta x\Delta y} + \dfrac{C_{1212}}{4\Delta x\Delta y}
\end{cases}
\qquad
\begin{cases}
h_{41} = \dfrac{C_{2212}}{2\Delta x\Delta y} \\[2mm]
h_{42} = \dfrac{C_{2222}}{\Delta y^2} - \dfrac{1}{2\Delta y}\left(\left(\dfrac{\partial C_{2212}}{\partial x}\right)_{ij} + \left(\dfrac{\partial C_{2222}}{\partial y}\right)_{ij}\right) \\[2mm]
h_{43} = -\dfrac{C_{2212}}{2\Delta x\Delta y} \\[2mm]
h_{44} = \dfrac{C_{1212}}{\Delta x^2} - \dfrac{1}{2\Delta x}\left(\left(\dfrac{\partial C_{1212}}{\partial x}\right)_{ij} + \left(\dfrac{\partial C_{2212}}{\partial y}\right)_{ij}\right) \\[2mm]
h_{45} = -\dfrac{2C_{1212}}{\Delta x^2} - \dfrac{2C_{2222}}{\Delta y^2} \\[2mm]
h_{46} = \dfrac{C_{1212}}{\Delta x^2} + \dfrac{1}{2\Delta x}\left(\left(\dfrac{\partial C_{1212}}{\partial x}\right)_{ij} + \left(\dfrac{\partial C_{2212}}{\partial y}\right)_{ij}\right) \\[2mm]
h_{47} = -\dfrac{C_{2212}}{2\Delta x\Delta y} \\[2mm]
h_{48} = \dfrac{C_{2222}}{\Delta y^2} + \dfrac{1}{2\Delta y}\left(\left(\dfrac{\partial C_{2212}}{\partial x}\right)_{ij} + \left(\dfrac{\partial C_{2222}}{\partial y}\right)_{ij}\right) \\[2mm]
h_{49} = \dfrac{C_{2212}}{2\Delta x\Delta y}
\end{cases}
\tag{B.5}
$$

Once the matrix M and the vector f have been constructed, the system can be solved and the residual stresses computed using the strain–displacement relationship and Hooke's law.

References

Ayad, M., Lapostolle, L., Rondepierre, A., Bras, C.L., Ünaldi, S., Donik, C., Klobcar, D., Berthe, L., Trdan, U., 2022a. New methodology of dynamical material response of dissimilar FSWed Al alloy joint under high strain rate laser shock loading. Mater. Des. 111080.

Ayad, M., Lapostolle, L., Rondepierre, A., Le Bras, C., Scius-Bertrand, M., Ünaldi, S., Trdan, U., Rouchausse, Y., Grassy, J., Maillot, T., Lapoujade, V., Michel, C., Berthe, L., 2022b. Modeling of multi-edge effects in the case of laser shock loadings applied on thin foils: Application for material characterization of aluminum alloys. J. Appl. Phys. 131 (9), 095902.

Benxin, W., Sha, T., Shuting, L., 2010. Numerical investigation of opposing dual sided microscale laser shock peening. J. Manuf. Sci. Eng. 256, 4376–4382.

Bhamare, S., Ramakrishnan, G., Mannava, S.R., Langer, K., Vasudevan, V.K., Qian, D., 2013. Simulation-based optimization of laser shock peening process for improved bending fatigue life of Ti–6Al–2Sn–4Zr–2Mo alloy. Surf. Coat. Technol. 232, 464–474.

Braisted, W., 1999. Finite element simulation of laser shock peening. Int. J. Fatigue 21 (7), 719–724.

Brockman, R.A., Braisted, W.R., Olson, S.E., Tenaglia, R.D., Clauer, A.H., Langer, K., Shepard, M.J., 2012. Prediction and characterization of residual stresses from laser shock peening. Int. J. Fatigue 36 (1), 96–108.

Bunge, H.J., 1982. Texture Analysis in Materials Science: Mathematical Methods, English ed Butterworths, London, Boston.

Case, S., Horie, Y., 2007. Discrete element simulation of shock wave propagation in polycrystalline copper. J. Mech. Phys. Solids 55 (3), 589–614.

Chen, H., Kysar, J.W., Yao, Y.L., 2004. Characterization of plastic deformation induced by microscale laser shock peening. J. Appl. Mech. 71 (5), 713–723.

Chen, H., Wang, Y., Kysar, J.W., Yao, Y.L., 2007. Study of anisotropic character induced by microscale laser shock peening on a single crystal aluminum. J. Appl. Phys. 101 (2), 024904.

Clauer, A.H., 2019. Laser shock peening, the path to production. Metals 9 (6), 626.

Clayton, J., 2005. Modeling dynamic plasticity and spall fracture in high density polycrystalline alloys. Int. J. Solids Struct. 42 (16–17), 4613–4640.

Ding, K., Ye, L., 2006. Physical and mechanical mechanisms of laser shock peening. In: Laser Shock Peening. Elsevier, pp. 7–46.

Fox, J.A., 1974. Effect of water and paint coatings on laser-irradiated targets. Appl. Phys. Lett. 24 (10), 461–464.

Ghoshal, G., Turner, J.A., 2009. Numerical model of longitudinal wave scattering in polycrystals. IEEE Trans. Ultrason. Ferroelectr. Freq. Control 56 (7), 10.

Harewood, F., McHugh, P., 2007. Comparison of the implicit and explicit finite element methods using crystal plasticity. Comput. Mater. Sci. 39 (2), 481–494.

Heuzé, T., 2017. Lax–Wendroff and TVD finite volume methods for unidimensional thermomechanical numerical simulations of impacts on elastic–plastic solids. J. Comput. Phys. 346, 369–388.

Hfaiedh, N., Peyre, P., Song, H., Popa, I., Ji, V., Vignal, V., 2015. Finite element analysis of laser shock peening of 2050-T8 aluminum alloy. Int. J. Fatigue 70, 480–489.

Huang, Y., 1991. A user-material subroutine incorporating single crystal plasticity in the ABAQUS finite element program. Mech. Rep. (178), 47.

Hutchinson, J.W., 1976. Bounds and self-consistent estimates for creep of polycrystalline materials. Proc. R. Soc. Lond. Ser. A Math. Phys. Eng. Sci. 348 (1652), 101–127.

Julan, E., 2015. Simulation Numérique Du Choc Laser Pour La Mise En Compression En Présence De L'état Initial Dû Au Soudage (Ph.D. thesis). Ecole Polytechnique.

Kanit, T., Forest, S., Galliet, I., Mounoury, V., Jeulin, D., 2003. Determination of the size of the representative volume element for random composites: Statistical and numerical approach. Int. J. Solids Struct. 40 (13–14), 3647–3679.

Lan, B., Lowe, M., Dunne, F., 2014. Experimental and computational studies of ultrasound wave propagation in hexagonal close-packed polycrystals for texture detection. Acta Mater. 63, 107–122.

Lapostolle, L., 2022. Etude Numérique De L'influence D'hétérogénéités Microstructurales Sur Les Contraintes Résiduelles Induites Par Choc Laser (Ph.D. thesis). Arts et Métiers, Paris.

Lapostolle, L., Derrien, K., Morin, L., Berthe, L., Castelnau, O., 2022a. Modeling and simulation of laser shock waves in elasto-plastic 1D layered specimens. Int. J. Solids Struct. 239–240, 111422.

Lapostolle, L., Morin, L., Derrien, K., Berthe, L., Castelnau, O., 2022b. Fast numerical estimation of residual stresses induced by laser shock peening. Eur. J. Mech. A Solids 104844.

Larson, E.A., Ren, X., Adu-Gyamfi, S., Zhang, H., Ren, Y., 2019. Effects of scanning path gradient on the residual stress distribution and fatigue life of AA2024-T351 aluminium alloy induced by LSP. Results Phys. 13, 102123.

Le Bras, C., Rondepierre, A., Seddik, R., Scius-Bertrand, M., Rouchausse, Y., Videau, L., Fayolle, B., Gervais, M., Morin, L., Valadon, S., Ecault, R., Furfari, D., Berthe, L., 2019. Laser shock peening: Toward the use of pliable solid polymers for confinement. Metals 9 (7), 793.

Lebensohn, R., Castelnau, O., Brenner, R., Gilormini, P., 2005. Study of the antiplane deformation of linear 2-D polycrystals with different microstructures. Int. J. Solids Struct. 42 (20), 5441–5459.

Leveque, R.J., 2002. Finite Volume Methods for Hyperbolic Problems. Cambridge University Press.

Lloyd, J., Clayton, J., Becker, R., McDowell, D., 2014. Simulation of shock wave propagation in single crystal and polycrystalline aluminum. Int. J. Plast. 60, 118–144.

Méric, L., Cailletaud, G., Gaspérini, M., 1994. F.E. calculations of copper bicrystal specimens submitted to tension-compression tests. Acta Metall. Et Mater. 42 (3), 921–935.

Morin, L., Braham, C., Tajdary, P., Seddik, R., Gonzalez, G., 2021. Reconstruction of heterogeneous surface residual-stresses in metallic materials from X-ray diffraction measurements. Mech. Mater. 158, 103882.

Peyre, P., Berthe, L., Vignal, V., Popa, I., Baudin, T., 2012. Analysis of laser shock waves and resulting surface deformations in an Al–Cu–Li aluminum alloy. J. Phys. D: Appl. Phys. 45 (33), 335304.

Peyre, P., Fabbro, R., Merrien, P., Lieurade, H., 1996. Laser shock processing of aluminium alloys. Application to high cycle fatigue behaviour. Mater. Sci. Eng. A 210 (1–2), 102–113.

Romanova, V., Balokhonov, R., Makarov, P., Schmauder, S., Soppa, E., 2003. Simulation of elasto-plastic behaviour of an artificial 3D-structure under dynamic loading. Comput. Mater. Sci. 28 (3–4), 518–528.

Schneider, Y., Weber, U., Wasserbäch, W., Zielke, R., Schmauder, S., Tillmann, W., 2020. A numerical method for the generation of hierarchical Poisson Voronoi microstructures applied in micromechanical finite element simulations—part I: Method. Comput. Mech. 66 (3), 651–667.

Seddik, R., Rondepierre, A., Prabhakaran, S., Morin, L., Favier, V., Palin-Luc, T., Berthe, L., 2022. Identification of constitutive equations at very high strain rates using shock wave produced by laser. Eur. J. Mech. A Solids 92, 104432.

Segurado, J., Lebensohn, R.A., 2021. An FFT-based approach for Bloch wave analysis: Application to polycrystals. Comput. Mech. 68 (5), 981–1001.

Sunny, S., Gleason, G., Bailey, K., Mathews, R., Malik, A., 2021. Importance of microstructure modeling for additively manufactured metal post-process simulations. Internat. J. Engrg. Sci. 166, 103515.

Thompson, R.B., Margetan, F., Haldipur, P., Yu, L., Li, A., Panetta, P., Wasan, H., 2008. Scattering of elastic waves in simple and complex polycrystals. Wave Motion 45 (5), 655–674.

Vukelić, S., Kysar, J.W., Lawrence Yao, Y., 2009. Grain boundary response of aluminum bicrystal under micro scale laser shock peening. Int. J. Solids Struct. 46 (18–19), 3323–3335.

Wang, Y., Kysar, J.W., Yao, Y.L., 2008. Analytical solution of anisotropic plastic deformation induced by micro-scale laser shock peening. Mech. Mater. 40 (3), 100–114.

Winey, J.M., LaLone, B.M., Trivedi, P.B., Gupta, Y.M., 2009. Elastic wave amplitudes in shock-compressed thin polycrystalline aluminum samples. J. Appl. Phys. 106 (7), 073508.

Xiang, Y., Mei, R., Wang, S., Azad, F., Zhao, L., Su, S., 2021. Numerical investigation of the effect of laser shock peening parameters on the residual stress and deformation response of 7075 aluminum alloy. Optik 243, 167446.

Zhang, K., Holmedal, B., Hopperstad, O., Dumoulin, S., Gawad, J., Van Bael, A., Van Houtte, P., 2015. Multi-level modelling of mechanical anisotropy of commercial pure aluminium plate: Crystal plasticity models, advanced yield functions and parameter identification. Int. J. Plast. 66, 3–30.

Zhang, P., Karimpour, M., Balint, D., Lin, J., 2012a. Three-dimensional virtual grain structure generation with grain size control. Mech. Mater. 55, 89–101.

Zhang, P., Karimpour, M., Balint, D., Lin, J., Farrugia, D., 2012b. A controlled Poisson Voronoi tessellation for grain and cohesive boundary generation applied to crystal plasticity analysis. Comput. Mater. Sci. 64, 84–89.

Zhang, W., Lawrence Yao, Y., 2001. Microscale laser shock processing—Modeling, testing, and microstructure characterization. J. Manuf. Process. 3 (2), 128–143.

Zhang, W., Yao, Y.L., Noyan, I.C., 2004. Microscale laser shock peening of thin films, part 1: Experiment, modeling and simulation. J. Manuf. Sci. Eng. 126 (1), 10–17.